

1
2
3
4
5
6
7
8
9
10
11
12
13
14
15
16
17
18
19
20
21
22
23
24
25
26
27
28
29
30
31
32
33
34
35
36
37
38
39
40
41
42
43
44
45
46
47
48
49
50
51
52
53
54
55
56
57
58
59
60

1 Nanoscale petrographic and geochemical insights on the
2 origin of the Palaeoproterozoic stromatolitic phosphorites
3 from Aravalli Supergroup, India

For Review Only

18 Reviewed manuscript to be re-submitted to *Geobiology*

ABSTRACT

Stromatolites composed of apatite occur in post-Lomagundi-Jatuli successions around 1.9 Ga and suggest the emergence of novel types of biomineralization at that time. The microscopic and nanoscopic petrology of organic matter in stromatolitic phosphorites might provide insights into the suite of diagenetic processes that formed these types of stromatolites. Correlated geochemical micro-analyses of the organic matter could also yield molecular, elemental, and isotopic compositions and thus insights into the role of specific microorganisms among these communities. Here, we report on the occurrence of nanoscopic disseminated organic matter in the Paleoproterozoic stromatolitic phosphorite from the Aravalli Supergroup of northwest India. Organic petrography by micro-Raman and Transmission Electron Microscopy imaging demonstrates syngeneity of the organic matter. Total organic carbon contents of these stromatolitic phosphorite columns are between 0.05 and 3.0 wt% and have a large range of $\delta^{13}\text{C}_{\text{org}}$ values with an average of -18.5‰ ($1\sigma = 4.5\text{‰}$). $\delta^{15}\text{N}$ values of decarbonated rock powders are between -1.2 to $+2.7\text{‰}$. These isotopic compositions point to the important role of biological N_2 -fixation and CO_2 -fixation by the pentose phosphate pathway consistent with a population of cyanobacteria. Microscopic spheroidal grains of apatite (MSGa) occur in association with calcite micro-spar in microbial mats from stromatolite columns and with chert in the core of diagenetic apatite rosettes. Organic matter extracted from the stromatolitic phosphorites contains a range of molecular functional group (e.g. carboxylic acid, alcohol, aliphatic hydrocarbons) as well as nitrile and nitro groups as determined from C- and N-XANES spectra. The presence of organic nitrogen was

independently confirmed by a CN- peak detected by ToF-SIMS. Nanoscale petrography and geochemistry allow for a refinement of the formation model for the accretion and phototrophic growth of stromatolites. The original microbial biomass is inferred to have been dominated by cyanobacteria, which might be an important contributor of organic matter and biomineralised early diagenetic phases to phosphorites in shallow-marine environments.

Keywords: phosphorite, stromatolites, Paleoproterozoic, carbonate, Aravalli, organic matter, Raman, FIB-SEM, STXM, ToF-SIMS, nano-petrology

1. Introduction

The distribution of phosphorites (phosphate deposits with more 15%wt P₂O₅) in the geological record is uneven and unlike that of any other sedimentary rock type. The oldest phosphogenic event in the Earth’s history took place during the late Paleoproterozoic (Papineau, 2010) and was followed by an even larger event of phosphate deposition during the latest Neoproterozoic and Cambrian (Norholt and Sheldon, 1986; Cook and Shergold, 1984). Both these events took place at times of increased oxygen availability in the atmosphere and oceans. Phosphatization thus appears to have been a consequence of atmospheric oxygenation, and as such might preserve a record of microbial activity in the newly oxygenated aqueous environments.

Evidence for microbial involvement in the formation of phosphorites includes the common occurrence of stromatolitic phosphorites (Shields et al., 1999; Sanchez-Navas et al., 1998; 2001; Krajewski et al., 2000; Banerjee et al., 1980). Layered shaly phosphorites from the early Neoproterozoic Torridonian Group are host to diverse communities of microorganisms (Battison and Brasier, 2012), including well-preserved Eukaryotic cells (Strother et al., 2011). Concretionary and finely laminated phosphorites from the Paleoproterozoic Zaonega Fm. preserve microscopic cylindrical and rounded structures that resemble methanotrophic and sulphur-oxidizing bacteria, consistent with a vent-seep-influenced environmental setting (Lepland et al., 2013). Microfossils and microbial fabrics have also been reported from phosphorites of all ages from a range of locations, including from the Paleoproterozoic Bijiki Fm. (Hiatt et al., 2015 and references therein). A recent report suggests the presence of Fe-oxidising bacteria in the Paleoproterozoic Jhamakotra phosphorites (Crosby et al., 2014).

Other unambiguous evidence for microbial involvement in the formation of phosphorites include organic-walled microfossils in the Neoproterozoic-Ediacaran of China (Xiao et al., 1998; She et al., 2014), the occurrence of pyritized microfossils in Tertiary and Neoproterozoic phosphorites (Cosmidis et al., 2013b; She et al., 2013), and the ubiquitous presence of finely disseminated organic matter in apatite in nearly all phosphorites. Phosphatized microbial cells have thus been reported in recent and ancient phosphorite deposits (e.g. O'Brien et al. 1981; Bertrand-Sarfati et al. 1997; Rao et al., 2000). Finally, while the debate on the original nature of the 'Doushantuo embryos' continues, these fascinating structures are certainly biological in origin (Xiao et al., 1998; Bailey et al., 2007; Xue et al., 1999; Hultgren et al., 2011).

Some details on the microscale structure of phosphorites have been unraveled using micro-analytical approaches (Sanchez-Navas et al., 1998; Cosmidis et al., 2013a; 2013b; She et al., 2013). Micron-size spheroidal apatites with nanoscale external layers of apatite of different crystal size or composition have been observed in fossilization experiments (Benzerara et al., 2004a), in Paleocene coprolitic phosphorite (Cosmidis et al., 2013a), and in Cretaceous stromatolitic phosphorites (Krajewski et al., 2000), all interpreted as phosphatized micro-organisms. In phosphorite crusts from the oxygen-minimum zone off the Peruvian shelf, nanoscopic spheroidal apatite structures have microbial morphologies and are closely associated with pyrite (Cosmidis et al., 2013b).

Nanoscale intracellular inclusions of carbonates have been reported from stromatolite-building cyanobacteria (Couradeau et al., 2012; Benzerara et al., 2014). Intracellular granules of poly-phosphate have also been reported from a range of cyanobacterial lineages (Benzerara et al., 2014). It thus appears plausible that cyanobacteria are capable of intracellular phosphatisation and thereby could become mineralogical cellular fossils. Could nanoscale petrographic and geochemical features of stromatolite growth or phosphatized microbial fossils be preserved in the Paleoproterozoic Aravalli stromatolitic phosphorites? The nanoscale petrology and geochemistry could have implications for the growth of stromatolites, the phylogenetic affinity of the inhabiting microorganisms, and the ecology of their microbial habitat after the Great Oxidation Event (GOE).

2. Samples and Geology

The Aravalli Supergroup of rocks from northwest India contains some of the oldest

1
2
3 112 and largest phosphate deposits of the Paleoproterozoic. The Aravalli phosphorites occur as
4
5
6 113 stromatolites in the Late Paleoproterozoic Jhamarkotra Formation, in the Aravalli
7
8 114 Supergroup (Banerjee, 1971; Chauhan, 1979; Roy and Paliwal, 1981; Sarangi et al., 2006;
9
10 115 Roy and Purohit, 2015). Recent geochronological analyses of poorly documented zircons
11
12 116 from the sandstones underlying these stromatolite reefs suggest that the Aravalli
13
14 117 stromatolitic phosphorites are younger than ca. 1.772 Ga (Mackenzie et al., 2013).
15
16 118 However this remains unconvincing because of the reasons discussed in Melezhik et al.
17
18 119 (2014) and also because of possible chemical and age zonations that have not been
19
20 120 documented in these alleged detrital zircons. In fact not even one zircon has been
21
22 121 documented to have a detrital morphology and/or a core of 1.772 Ga without later
23
24 122 metamorphic zircon overgrowth. Distinctive carbon and nitrogen isotope compositions
25
26 123 vary between 'basins' which have locally unique geochemical and mineralogical
27
28 124 compositions (Papineau et al., 2009; 2013; Purohit et al., 2010; 2012). While rocks
29
30 125 associated with phosphate are contemporary to the rocks with ^{13}C -enriched carbonates, as
31
32 126 they are indeed most likely younger than the Lomagundi-Jatuli Event (LJE) that ended at
33
34 127 2.06 Ga (Papineau et al., 2013). Clearly as repeatedly stated in McKenzie et al. (2014),
35
36 128 more stratigraphy and geochronology remains to be investigated to confirm that the
37
38 129 Jhamarkotra stromatolitic phosphorites are younger than 1.772 Ga and separately, that the
39
40 130 Jhamarkotra formation was deposited during a hypothetical latest Paleoproterozoic $\delta^{13}\text{C}_{\text{carb}}$
41
42 131 excursion (Mackenzie et al., 2013; 2014; cf. Melezhik et al., 2014).
43
44
45
46
47
48
49
50

51
52 132 Characteristic carbonate carbon isotope compositions vary between 'basins' where
53
54 133 the geochemical and mineralogical compositions of organic carbon are locally unique.
55
56 134 These geochemically distinct marine sedimentary environments have been contrasted
57
58
59
60

1
2
3
4
5
6
7
8
9
10
11
12
13
14
15
16
17
18
19
20
21
22
23
24
25
26
27
28
29
30
31
32
33
34
35
36
37
38
39
40
41
42
43
44
45
46
47
48
49
50
51
52
53
54
55
56
57
58
59
60

135 before with various geochemical proxies and thus are discussed here again as rocks
136 associated with phosphorites, referred to as the ‘Phosphate Domain’, and rocks that are
137 associated with $\delta^{13}\text{C}_{\text{carb}}$ excursions, as the ‘Non-Phosphate Domain’ (Papineau et al., 2009;
138 2013; Purohit et al., 2010; 2012).

139 The closing of the Aravalli Epeiric Sea and eventually of the Udaipur Epicontinental
140 Sea under increasingly oxygenated conditions, might have been responsible for near-ideal
141 conditions for the formation, accumulation, and preservation of stromatolitic phosphorites.
142 The paleoenvironments proposed for the Aravalli stromatolitic phosphorites include
143 oceanic embayment, epicontinental sea, lagoon, or tidal shallow-marine environments (Roy
144 and Jakhar, 2002, Roy and Paliwal, 1981). This geographically restricted
145 paleoenvironment might have developed during the earliest phase of the Aravalli orogeny,
146 which started before the emplacement of the Berach granite, after the successive
147 development of the other regional rift basins along the paleo-margin of the Archean Mewar
148 Gneiss Complex.

149 The finely laminated columnar stromatolites are mainly composed of carbonate
150 fluorapatite and dolomite and form a band about 35m in thickness in the dolomite unit of
151 the Jhamarkotra Formation in the Jhamarkotra mine (JK-samples). Near the Badagaon
152 village (N: 24°37'17.9"; E:73°40'44.8"), in the likely synchronous Udaipur Valley (UV-
153 samples), the stromatolitic phosphorite horizon is structurally complex (unmapped) and
154 possibly repeats in the massive embedding dolomite. Weathered surfaces in the field show
155 alternating high and low relief caused by the differential weathering of carbonate-
156 fluorapatite and dolomite, respectively (Fig. 1). Samples in this study came from a quarry
157 near the village of Badagaon in the northwestern part of the city of Udaipur, from the

Jhamarkotra embayment to the east, and also include associated black shales (Table 1). We use a correlated micro-analytical approach to determine the petrological and geochemical nature of micro- and nanoscale structures in the stromatolitic phosphorites.

3. Analytical techniques

3.1. Microscopy and Raman micro-spectroscopy

Optical microscopy was performed with an Olympus Bx51 microscope with 4X, 10X, 20X, 50X, and 100X (with a 1.0mm working distance) objectives on 30 μm thin sections polished with 0.25 μm Al_2O_3 . No oil immersion was used. Raman microspectroscopic imaging was performed with a WITec Confocal Raman Imaging system using a 532 nm laser at up to 1000X magnification. An optic fiber 50 microns in diameter was used to collect a Raman spectrum for each pixel (360 x 360 nm) with a dwell time of 0.6 seconds. Raman spectral images of mineral associations were generated by mapping peak intensity for specific chemical bonds in minerals from each spectral scan using a data acquisition and processing software (Papineau et al., 2010a; Bernard et al., 2008).

3.2. Isotope Ratio Mass Spectrometry (IRMS)

The carbon isotope composition of organic matter was measured in micro-drilled powders from slabs of stromatolitic phosphorites. Micro-drilled powders were obtained from slabs of the Aravalli stromatolitic phosphorites and were de-carbonated in phosphoric acid at 70°C overnight for the carbonate stable C and O isotope analyses. A TiN drill bur two millimeters in diameter was used to collect powder from the sub-surface of the slab, the latter of which was used for organic C and N isotopes. Considering the high

hardness of TiN, the relative softness of phosphorites, and the absence of N in powders micro-drilled from hard cherts selected for tests, it is highly unlikely that the bur is a source of contamination for our N analyses. Powders were collected onto muffled aluminum foil and poured into muffled glass vials (550°C for at least 4 hours) until analysis. Total nitrogen and organic carbon analyses were performed with a Costech ECS 4010 elemental analyzer (EA) linked to a Thermo Fischer Delta V IRMS through a Conflo IV interface. Powdered samples were weighed in muffled Ag boats (around 5 mg of powder) for decarbonation with ultrapure 6N HCl (Sequanal Grade, Thermo Scientific). Decarbonated samples were then introduced by the EA autosampler for combustion at 1020°C in the presence of ultrapure O₂. Long-term tests (>12 months) on the NBS 22 (of the National Bureau of Standards) standard give reproducibility better than ±0.1‰ for δ¹³C; acetanilide reference material gave reproducibility of ±0.3‰ for δ¹⁵N, and an analytical precision for abundances better than ±5%. Carbon and nitrogen isotope data are reported in the conventional form $\delta^{13}\text{C}_{\text{org}} = [({}^{13}\text{C}/{}^{12}\text{C})_{\text{microdrillate}}/({}^{13}\text{C}/{}^{12}\text{C})_{\text{PDB}} - 1] \times 1000\text{‰}$ and $\delta^{15}\text{N} = [({}^{15}\text{N}/{}^{14}\text{N})_{\text{WR}}/({}^{15}\text{N}/{}^{14}\text{N})_{\text{air}} - 1] \times 1000\text{‰}$. Stable isotope data for Udaipur Valley stromatolitic phosphorites are compared to those of Jhamarkotra, Jhabua, and Sallopat, and to the carbonates and shales from both the ‘Phosphate Domain’ and the ‘Non-Phosphate Domain’. Bulk major, minor and trace element analyses were performed as previously described (Papineau et al., 2013).

3.3. Scanning Electron Microscopy (SEM) – Focused Ion Beam (FIB)

Focused ion beam (FIB) milling and lift-out were performed with a JEOL JIB 4500 MultiBeam system equipped with an Evactron system. Polished thin sections were first

covered with a ca. 10 Å gold-coat, inserted into the FIB-SEM, and a W shield was then deposited on the surface of the target prior to milling. A focused 30 keV Ga⁺ primary beam was then used to sputter away material from both sides of the deposited W shield. A lamella was then nano-fabricated in the following general sequence of steps: 1) mill out and expose the target, 2) lift-out and weld the lamella with W to a Cu TEM half-grid, and finally, after cutting the needle, 3) thin down with progressively smaller beam currents (down to 20 pA). For this work, a lamella of about 14.6 x 8.3 µm and 120 nm in thickness was nano-fabricated. More details about the FIB technique can be found described in Wirth (2009) and Zega et al. (2007).

3.4. Transmission Electron Microscopy (TEM)

High resolution TEM analysis of the lamella was performed with a 200 keV JEOL JEM-2500SE at the Astromaterials Research and Exploration Science e-beam facility at NASA Johnson Space Center and with a 200 keV JEOL JEM 2100 in the Department of Chemistry at University College London. Detailed mineralogy of the FIB lamella was characterized in both bright imaging mode and in scanning (STEM) mode using both bright-field (BF, unscattered electrons) and dark field (DF-scattered electrons) STEM detectors. Individual grains of apatite, carbonate, and organic inclusions were distinguished primarily by energy dispersive X-ray spectroscopy (EDS) with a Noran spectrometer, acquired in STEM mode. The TEM at UCL uses a field emission LaB₆ electron source and is equipped with an Oxford Instruments 80 mm² silicon drift EDS detector. High-resolution imaging by STEM-BF and DF was performed with a spot size of 0.7 nm, and

by X-ray detections by the EDS detector, which are correlated to the STEM scan coils, thereby enabling compositional mapping of the target at sub-nm spatial scales.

3.5. Synchrotron-based Scanning Transmission X-ray Microscopy

Sample preparation for X-ray absorption near-edge structure (XANES) spectral analysis involved dissolution of whole-rock powder from stromatolitic phosphorites either with 9 N HF:1 N HCl or with a CsF-HF solution treatment (Alexander et al., 2007). Dissolved powders were thus treated in this CsF solution with a density set at about 1.8 g/cm³. Dioxane was then used to generate a separate solution of lower density, which floats on top of the CsF in a teflon tube. The acid insoluble organic matter liberated from this treatment float at the interface between the two solutions. After centrifugation, the acid insoluble organic matter was pipetted in muffled glass vials, rinsed several times in 2 M HCl, washed in DI water, and finally dried in air. Once dried, small clumps of organic matter were mixed with molten sulphur (~80°C) that form a bead on a glass slide. Upon cooling, the sulphur crystallizes and traps the acid insoluble organic matter. The sulphur bead was subsequently detached from the glass slide and glued onto an epoxy stub and microtomed with a diamond knife into 100 nm slices. Microtome sections of powdered acid-insoluble organic matter were transferred to 200 mesh, thin bar, Cu TEM grids coated with silicon monoxide. The sulphur was removed by evaporation by exposing the grid to ~70°C of air for a few minutes over a hot plate.

Samples were analyzed with the polymer STXM beamline 5.3.2.2. at the Advanced Light Source (ALS), Lawrence Berkeley National Laboratory (Kilcoyne et al., 2003). During analysis the electron current in the storage ring was held constant in “topoff mode” at 500

mA at energy of 1.9 GeV, providing a constant flux of photons at the STXM end-station. The dispersive and non-dispersive exit slits were set at 25 μm . Focusing of the photon beam is produced by a Fresnel zone plate with a spot size of around 30 nm. STXM data were acquired as spectral image stacks (i.e. a series of X-ray absorption images at sequential energies), from which XANES spectra of regions of interest were extracted. The highest spectral resolution (0.1 eV step between subsequent images) was in the 282-292 eV range, where the near-edge spectral features for electronic transitions from core shell states to anti-bonding σ^* and π^* -orbitals are located. XANES spectra are presented as the ratio of transmission spectra from the region of interest, I , relative to background transmission spectra, I_0 , calculated as $A = -\ln(I/I_0)$.

3.6. Time-of-Flight Secondary Ion Mass Spectrometry

Analyses of the FIB lamella by ToF-SIMS were performed with an IONTOF SIMS V instrument located in the Department of Materials at Imperial College. Mass spectra were collected using a 0.1 pA Bi_3^+ primary beam current (at the sample), after cleaning of the FIB lamella surface with the ion beam, and ensuring the ion signals were stable. Organic contamination of the surface of the FIB lamella was already minimized using an Evactron pre-cleaned sample chamber of the FIB. During analysis, atoms from the specimen are sputtered and ionized from the sample, and accelerated by 25 keV into the Time-of-Flight analyzer and counted in the detector. The travel time of the secondary ions is proportional to the square root of their mass and thus a mass spectrum is generated. The detector of ToF instruments has a high mass resolution, typically a $M/\Delta M$ greater than 10000, and the detection limit is in the femtomole level. For surface ion mapping the primary ion beam is

1
2
3
4
5
6
7
8
9
10
11
12
13
14
15
16
17
18
19
20
21
22
23
24
25
26
27
28
29
30
31
32
33
34
35
36
37
38
39
40
41
42
43
44
45
46
47
48
49
50
51
52
53
54
55
56
57
58
59
60

272 rastered over the surface of the sample with a spatial resolution down to about 50 nm. The
273 ToF-SIMS technique allows for *in situ* analysis of molecules with up to several thousand
274 AMU. To our knowledge, this is the first time that ToF-SIMS analyses of FIB lamellae have
275 been reported, and we show that such an instrument can provide independent
276 confirmation of nano-petrological and geochemical data.

277
278 **4. Results**

279 **4.1. Petrology and organic crystallinity**

280 There are two main phases that compose stromatolitic phosphorites: carbonate and
281 carbonate-fluorapatite (apatite from hereon; Fig. 1). Stromatolite columns are dominated
282 by apatite, whereas the intercolumnar space is dominated by dolomite (Fig. 1, 2a). Convex
283 upward alternating laminations of apatite and carbonate in the stromatolite columns
284 usually vary between 1-3 mm thick at Badagaon and Jhamarkotra (Fig. 1). Laminations
285 also occur at the centimeter, millimeter, and micron scales. Organic matter is concentrated
286 in specific layers (Fig. 2g-h). In the intercolumnar dolomite, there are rounded
287 microstructures that preserve organic matter in apatite (Fig. 2a-d). In fact they form
288 millimeter-scale fields with hundreds of discrete apatite rosettes (Fig. 3) that contain a core
289 of chert with inclusions of microscopic spheroidal grains of apatite (MSGA from hereon;
290 Fig. 2e, f). In polished slabs, the apatite columns appear dark to light gray and the
291 intercolumns usually have a lighter gray with occasional patches stained by Fe-oxides (Fig.
292 4).

293 Syngenecity of the organic matter is confirmed by micro-Raman imaging, which
294 shows the systematic presence of nanoscale inclusions of organic matter in apatite,

including in MSGA (Fig. 5). From its Raman spectra, the organic matter could be described as graphitic carbon qualitatively consistent with greenschist facies metamorphism. In a preserved microbial mat from a stromatolitic column at Badagaon, the fine organic-rich laminations occur almost exclusively in association with apatite (Fig. 5j-l). Organic-rich apatite layers are interlayered with carbonate layers, both typically around 10 μm in thickness (Fig. 2e, 2h, 5k). These characteristics collectively support that the nanoscale inclusions of graphitic carbon are indigenous and syngenetic and that there are features from the depositional environment preserved in these rocks.

In comparison, in the rounded rosette-like structures of the inter-columnar dolomite, organic matter occurs predominantly in the apatite outer layer of the rosette and in the core of chert (Fig. 5a-i). These rosette structures are locally abundant in intercolumnar areas and about 40% of them occur as individual microstructures while the others occur in small clusters of two to six rounded microstructures (Fig. 3, 5). Individual rosette-like microstructures have sizes that vary between 50 and 120 μm , while clusters vary between 60 and 240 μm . Microstructures contain finely disseminated organic matter predominantly in their outer layers, typically 15 to 25 μm in thickness, but also in their central cherty areas (typically about 10 to 30 μm in size). Organic matter also rarely occurs in the surrounding dolomite matrix, although in significantly lower abundance. These observations demonstrate that organic matter is intimately associated with apatite and that both these phases formed syngenetically.

Raman spectra of organic matter have low ratios of D-band to G-band areas, varying between 0.57 and 0.64 (Table 2). The G- and D-bands peak at 1575 cm^{-1} and 1346 cm^{-1} , respectively and have FWHM between 10 and 17 (red spectra in Fig. 5). Because the

1
2
3 318 crystallinity of the organic matter relates to the highest temperature the rock was exposed
4
5
6 319 to (Beyssac et al., 2002), calculations of the estimated crystallisation temperature yields
7
8 320 $470 \pm 50^{\circ}\text{C}$ according to the Beyssac geothermometer. Raman spectra for carbonates
9
10 321 show the main C-O peak at 1096 cm^{-1} (Table 2), which is more in line with the detection of
11
12 322 dolomite than calcite that has its main C-O Raman peak at slightly lower wavenumbers
13
14 323 (typically $1083\text{-}1087\text{ cm}^{-1}$). Raman measurements did not resolve the presence of calcite
15
16 324 from dolomite, possibly due to phase overlap at the scale near the spatial resolution of the
17
18 325 instrument. The main P-O peak for apatite in the Badagaon stromatolites was measured at
19
20 326 964 cm^{-1} , and was notably always associated with the D- and G-band peaks of graphitic
21
22 327 carbon (Fig. 5). Our Raman data are collectively consistent with a syngenetic origin for
23
24 328 Aravalli organic matter.
25
26
27
28
29
30
31
32

33 330 **4.2. Stable isotope compositions of carbon and nitrogen**

34
35 331 The Badagaon intercolumnar carbonate $\delta^{13}\text{C}_{\text{carb}}$ values are close to 0‰ , whereas the
36
37 332 $\delta^{13}\text{C}_{\text{carb}}$ values for columnar carbonate-apatite are slightly more negative by $1\text{-}2\text{‰}$ than
38
39 333 values for intercolumnar carbonate, which is similar for Jhamarkotra stromatolitic
40
41 334 phosphorites (Fig. 6a). The content of organic carbon varies significantly between 0.1 and
42
43 335 3.0 \%wt (Fig. 6c), and columnar regions generally contain more organic matter than the
44
45 336 intercolumnar regions, which independently confirms petrographic observations by
46
47 337 transmitted light microscopy and micro-Raman. De-carbonated microdrilled powders
48
49 338 from Badagaon (Udaipur Valley; Fig. 6a) have a large range of $\delta^{13}\text{C}_{\text{org}}$ values between -32.2
50
51 339 and -13.0‰ (excluding a single analysis at -39.4‰), which yields an average of -18.5‰
52
53 340 ($1\sigma = 4.5\text{‰}$). This range of $\delta^{13}\text{C}_{\text{org}}$ values is slightly larger than previously reported,
54
55
56
57
58
59
60

although ^{13}C -enriched organic matter is known to occur in the Jhamarkotra stromatolitic phosphorites (Papineau et al., 2013; Sreenivas et al., 2001; Banerjee et al., 1986). Organic matter from decarbonated microdrilled powders has a large range of $\delta^{13}\text{C}_{\text{org}}$ values between about -12 and -39.4‰ (Fig. 6b). We note that only one out of eleven isotopically light $\delta^{15}\text{N}$ values detected in decarbonated microdrilled powders does not occur in the intercolumnar space (Table 3, Fig. 6c).

Nitrogen abundances in the stromatolitic phosphorites are between 0.03 and 0.11 %wt (Table 3), whereas $\delta^{15}\text{N}$ values are low and sometimes negative, between -1.2 and +2.7‰ (Fig. 6c). Stromatolitic phosphorites in Badagaon have similar N concentrations and $\delta^{15}\text{N}$ values as other phosphorites and carbonates from the Udaipur Valley (N = 0.03 to 0.09 %wt and $\delta^{15}\text{N}$ = 0.0 to +2.3‰), Kanpur (N = 0.02 to 0.03 %wt and $\delta^{15}\text{N}$ = 0.0 to +3.4‰), and Dakankotra (N = 0.03 to 0.09 %wt and $\delta^{15}\text{N}$ = +0.7 to +3.1‰), but different from the stromatolitic phosphorites from the Jhamarkotra mine area in which no N was detected (Fig. 6e; Papineau et al., 2013). We note that only one out of eleven isotopically light $\delta^{15}\text{N}$ values detected in decarbonated microdrilled powders does not occur in the intercolumnar space (Table 3).

In comparison, stratigraphically overlying carbonaceous shales from Amberi village, east of Badagaon in the Udaipur Valley have C:N_{AT} ratios greater than 10 and generally > 100 (Fig. 6e; Papineau et al., 2009). The C:N_{AT} in shales overlying the ^{13}C -enriched carbonates from Ghasiar and Rama in the older Non-Phosphate Domain are < 50 (Fig. 6e). With slightly negative $\delta^{15}\text{N}_{\text{TN}}$ values, the Badagaon stromatolitic phosphorites have N compositions similar to the carbonates, but not to the shales, of both the Phosphate Domain (PD) and the Non-Phosphate Domain (NPD) (Fig. 6e).

4.3. Ultrastructure of a microbial mat in Badagaon stromatolitic phosphorite

In a rare microbial mat that composes the stromatolitic columns of apatite, layers of MSGA and calcite occur in succession with ~10 µm spacing between repeayed layers (Figs. 2h and 7f). Layers of apatite are thus sandwiched between layers of calcite (Fig. 8c-d). Apatite in MSGA is systematically peppered with nanoscopic inclusions of organic matter and carbonate (Fig. 8f-h and 9a-c). When MSGA occur in the carbonate interlayers, it is associated with calcite micro-spar, which form extensions or protuberances thus composed of apatite and calcite. These extensions are radiating outwards from the curvature of the microbial mats (Fig. 2h). The space between these extensions and layers is filled with later diagenetic dolomite sometimes with a characteristic curvy-linear network pattern (Fig. 8i).

A few nanoscopic globular structures in MSGA were observed (Fig. 8e) to be similar to nanoscale electron-lucent features reported from micron-size euhedral apatite from Jurassic stromatolitic phosphorites from Spain (Fig. 5 in Sanchez-Navas et al., 1998). Microscopic apatite with rounded electron-lucent centers within the phosphate crystals produced under electron bombardment during TEM analysis have been interpreted as the result of a release of volatile compounds (OH⁻, Cl⁻, F⁻; cf. Sanchez-Navas et al., 1998). Therefore we interpret these electron-lucent structures are likely caused by electron beam damage, also in analogy to electron beam damaged quartz that occurs as strain contrast centres (Martin et al., 1996; Carter and Kohlstedt, 1981).

4.4. Elemental and molecular compositions of Aravalli stromatolitic phosphorites

The abundance of P₂O₅ and SiO₂ is highly variable in the stromatolitic phosphorites

analysed and up to 28.3% and 34.59%, respectively (Table 3). Abundances of Mn in analysed microdrilled powders ($n = 4$) vary between 244 and 1364 ppm, which yields low Mn/Sr between 1.1 to 14.3 (Table 3). Processes of diagenesis, metamorphism, and hydrothermal circulation can all affect carbonate mineralogy and lower $\delta^{13}\text{C}$ and $\delta^{18}\text{O}$ values as well as introduce Mn and remove Sr (Nabelek et al., 1991). The measured range of Mn/Sr between 1.1 and 14.3 is low and thus considered here to be largely unaltered. However, Mn/Sr ratios greater than 10 (Kaufman and Knoll, 1995) or 6 (Melezhik et al., 1999) are considered to imply significant post-depositional alteration. Therefore, conservatively, only two bulk powders have Mn/Sr less than 6 and preserve pristine isotope compositions.

A layer of apatite was nano-fabricated into a FIB lamella of a microbial mat in the stromatolitic columns from a stromatolitic phosphorite at Badagaon. Layers of MSGA are sandwiched between two layers of calcite which did not contain Mg, Mn, or Fe (Fig. 8c-d). Apatite in MSGA is systematically peppered with nanoscopic inclusions of organic matter and carbonate (Fig. 8f-h and 9a-c). Major elements identified by EDS in the layers of the microbial mats include Ca, Mg, P, C, and O, in relative proportions indicative of apatite, calcite, and dolomite (Fig. 8b). Beside trace levels of Si in all phases, Cl and F were detected in the apatite, and Fe was detected in dolomite (Fig. 8b).

Acid-insoluble organic residues analyzed by synchrotron-based STXM contain various molecular functional groups in Aravalli stromatolitic phosphorites (Fig. 10). Carbon-XANES spectra reveal aromatic carbon ($\text{C}=\text{C}$) bonding that corresponds to the bound states of π^* (285.3 eV) and σ^* (291.7 eV) electronic orbitals. While contributions from both alkenyl or aromatic moieties can contribute to these peaks, the characteristic

1
2
3
4
5
6
7
8
9
10
11
12
13
14
15
16
17
18
19
20
21
22
23
24
25
26
27
28
29
30
31
32
33
34
35
36
37
38
39
40
41
42
43
44
45
46
47
48
49
50
51
52
53
54
55
56
57
58
59
60

excitonic structure of the σ^* peak indicates the presence of planar domains of highly conjugated graphene sheets (Cody et al., 2008). Absorption features between these two energies are caused by the presence of molecular functional groups in the organic matter. In particular, XANES spectra at the C-edge reveal aliphatic C-C bonds (287.6 eV), nitrile, ketones or aromatic alcohol functional groups (286.7 eV), carboxylic acid (288.5 eV), and alcohol or hydroxylated aliphatic carbon (289.4 eV) (Table 4). Unfortunately, the spectra at the C, N, and O edges were collected at different times over two analytical sessions, and therefore, cannot reliably be used to independently estimate C:N_{AT} and C:O_{AT} ratios.

Nitrogen-XANES spectra of microtomed organic matter extracted from powdered bulk stromatolitic phosphorite show a resolved N edge (Fig. 10), which confirms the presence of nitrogen in the organic phase. The XANES spectra at the N- and O-edges show the presence of nitrile peaks at 399.8 eV and reveal the presence of amidyl or peptidyl groups (401.1 eV), nitro-compounds (404.5-405.0 eV), and ketones (531.4 eV) (Cody et al., 2011; Leinweber et al., 2007). In comparison, acid-insoluble organic matter from carbonaceous shales in the ‘phosphate domain’ (UV0606, UV0609, DD-1, AB-3) have peaks at 399.6 eV, 400.9 eV, 403.7 eV and 404.5 eV (Fig. 11) representing similar molecular functional groups (Table 4). We note that the observed bonds sometimes occur in organic matter from carbonaceous shales from both the ‘phosphate domain (PD)’ and ‘non-phosphate domain (NPD)’ (GH-4, UM-4, RM-3, RM-5, and GH-14; Fig. 11).

Positive and negative secondary ion analyses of the FIB foil by ToF-SIMS show that small organic and inorganic fragments can be also detected *in situ* by ToF-SIMS and independently validate our XANES and TEM-EDS *in situ* data (Fig. 12). A range of peaks from the known elements that compose the minerals apatite, calcite, and dolomite include:

H⁻, C⁻, O⁻, F⁻, Mg⁺, P⁻, Cl⁻, and Ca⁻ (Table 5). Many isotopes of these elements have also been detected and they have also been identified in molecular fragments from apatite (PO⁻, CaP⁻, PO₃⁻, CaPO₂⁺, Ca₂PO₃⁺, Ca₂PO₄⁺, Ca₃PO₅⁺, Ca₄PO₆⁺, Ca₅PO₇⁺, Ca₆PO₈⁺, Ca₅P₃O₁₂⁺, Ca₆P₃O₁₃⁺, Ca₇P₃O₁₄⁺, Ca₈P₃O₁₅⁺, Ca₉P₃O₁₆⁺; Fig. 12b; Table 5). These are similar to the several groups of peaks with masses >100 amu that are consistent with the secondary ionisation of apatite observed in tooth and bones (Malmberg et al., 2007). Another notable molecular fragment is the CN⁻ peak at mass 26 (Fig. 12a), which could also contain some contribution from C₂H₂, is unlikely to be a contaminant as it is expected to occur from nitrile functional groups independently visualized at the N 1s edge in associated sample UV0603 (Fig. 10).

A few contaminants were detected that originated from the nano-fabrication by FIB including Cu and Ga. However, no typical contaminants (polydimethylsiloxane – Thiel and Sjoval, 2011) were detected from the nano-fabricated FIB lamella in our negative or positive secondary ion spectra. Several ToF-SIMS peaks remain unidentified. XANES spectra at the Ca-2,3P edge for calcite and apatite (Fig. 9g) show identical patterns of peaks to those of calcifying cyanobacteria during experimental phosphatization experiments (Benzerara et al., 2004b). While secondary ion data of these molecular fragments decidedly confirm our previous results by STEM-EDS (Fig. 8c-d) and STXM at the C1s and Ca2p edges (Fig. 9f-h), ToF-SIMS maps of Ca and Mg show the details of the structure of the microbial mat (Fig. 12f).

5. Discussion

5.1. Diagenetic processes and apatite rosettes

1
2
3
4
5
6
7
8
9
10
11
12
13
14
15
16
17
18
19
20
21
22
23
24
25
26
27
28
29
30
31
32
33
34
35
36
37
38
39
40
41
42
43
44
45
46
47
48
49
50
51
52
53
54
55
56
57
58
59
60

The nanoscale structure of Aravalli stromatolitic phosphorite in Badagaon demonstrates a high degree of preservation of early diagenetic products. The Badagaon stromatolitic phosphorites are oriented, densely packed, columnar stromatolites that have occasional branches. Centimeter-size stromatolites branches likely formed sub-aqueous in the photic zone of the redox transition or oxygen minimum zone. The new observations reported here, show that microscopic and nanoscopic mineral assemblages are preserved soon after sedimentation and that burial could have been more rapid during times of higher phosphate availability.

In simulated diagenetic experiments on organic matter, the $\delta^{13}\text{C}_{\text{org}}$ and $\delta^{15}\text{N}_{\text{org}}$ values change by less than 4‰ (Lehmann et al., 2002). It is likely that, even if combined with small fractionation induced by lower greenschist facies metamorphism, the C isotope compositions of Udaipur Valley stromatolitic phosphorites closely reflect those acquired during deposition and early diagenesis. In fact, early diagenetic fractionation effects are preserved in the apatite-rich stromatolite columns, which have lower $\delta^{13}\text{C}_{\text{carb}}$ values than the intercolumnar carbonate and can be attributed to both early diagenetic calcite and dolomite cement (Table 2, Fig. 5a).

The rosettes described in stromatolitic phosphorites from Badagaon have a range of sizes and slightly different morphologies that make them inconsistent with an interpretation as microfossils. They have the same sizes and morphologies as the microstructures previously described as “coccoid-like algal forms” (Chauhan, 1979). Specifically he states:

“They are mainly of two types: (1) Cells are spheroidal to ellipsoidal in shape and range in diameter from 30 to 48 μm (max. diam.), with an average diameter of 38 μm . Some of the

cells show dense organic material in their centre. Cell walls appear hazy and are marked by finely disseminated organic material (Fig. 17). (2) Cells are bigger than (1) having diameters (max.) from 80 to 125 μm and show distinct cell walls of 6-8 μm thickness. Some of the cells contain centrally positioned prominent dark inclusions. M.R. Walter (pers. comm.) is of the view that these bigger cellular structures are likely to be partly preserved algal colonies rather than single cells and their inclusions actually represent numerous remnants of 5-10 μm wide cells (Fig. 18). Most of the cellular structures appear deformed from elliptical to irregular shapes and become undecipherable (Fig. 17)."

Based on our observations, we conclude that we are describing similar structures. However, the apatite rosettes are located only in the intercolumnar space and have a range of sizes inconsistent with most cyanobacteria, including the large cyanobacterium *Chroococcus* sp. A more likely relevant comparison is with the product of long-term diagenetic experiments at 25°C on apatite that have shown the formation of radially fibrous rosette-like apatite, sometimes also as dumbbell shaped microscopic structures (Blake et al., 1998). Other diagenetic experiments with conditions set at 170°C and 1.2 kbar on the oxidation of organic matter by ferrihydrite have also produced rounded, rosette-like, micro-structures composed of siderite (Kohler et al., 2013). Apatite rosettes have also been reported from the organic-rich cherts of the Late Paleoproterozoic FB Formation in the Francevillian Supergroup from Gabon (Mossman et al., 2005) and in Neoproterozoic phosphorites from China (Sun et al., 2014). The former rosettes form sedimentary bands and are composed of apatite at the center, rimmed by quartz and embedded in a matrix of siderite and stilpnomelane (Mossmann et al., 2005). Similar jaspilite-siderite rosettes with apatite cores have also been described in a banded iron formation and have been

1
2
3
4
5
6
7
8
9
10
11
12
13
14
15
16
17
18
19
20
21
22
23
24
25
26
27
28
29
30
31
32
33
34
35
36
37
38
39
40
41
42
43
44
45
46
47
48
49
50
51
52
53
54
55
56
57
58
59
60

considered as non-biological (Heaney and Veblen, 1990) whereas, other sideritic micro-spheres from the Gunlfint formation have been interpreted as biological-eukaryotic in origin (Kazmierczak, 1979). In light of these observations and experiments, a diagenetic concretionary-type origin is favored for the rosettes observed in Badagaon. Direct microbial involvement in the formation of these rosette structures, however, remains to be evaluated.

Papineau et al. (2013; 2009) argued that evidence for high productivity in the Lower Aravalli Group is variably preserved in the NPD as high $\delta^{13}\text{C}_{\text{carb}}$ values in carbonates, and in the PD as high $\delta^{13}\text{C}_{\text{org}}$ values of organic matter and high organic content of shales. It is therefore perhaps not surprising to see apatite rosettes in the Udaipur stromatolitic phosphorite environment, where diagenetic processes were naturally associated with high productivity. While diagenetic processes usually involve sulphate-reducing bacteria that produce isotopically light bicarbonate and hydrogen sulphide (if sulphate concentration are higher than about 200 μM – Habicht et al., 2002), very few sulphide minerals occur in our samples, perhaps due to a lack of ferrous Fe in the PD. The new observations presented here are similar to experiments in which early diagenetic concretionary apatite structures can form under similar conditions as in the intercolumnar space of stromatolitic phosphorites. We thus hypothesize that the apatite rosettes formed during diagenesis, but because they contain an indigenous core of chert, we further hypothesise that rosette cores formed from pelagic clumps of phosphatising microorganisms bonded in extracellular polymeric substances (EPS), which silicified early.

5.2. Microfossils(?) and taphonomy in phosphorite

The degree of preservation of the Aravalli stromatolitic phosphorites is indicated by early diagenetic textures, crystal sizes, and the degree of ordering of the organic matter (Banerjee, 1980). Raman spectra show that organic matter is well-preserved and relatively crystallized, although not completely graphitized. Raman spectra for organic matter (Fig. 5) show that it is systematically associated with apatite, which implies that C in the graphitic carbon and P in the apatite both cycled through microorganisms prior to lithification. In fact, Raman spectra show that the organic matter has spectral characteristics consistent with greenschist facies metamorphism, and therefore is considered indigenous and syngenetic.

The central chert core of the apatite rosettes from Badagaon is host to microscopic spheroidal grains of apatite (MSGa; Fig. 2e-f), which are identical to the microscopic spheroidal grains of apatites seen in microbial mats within the stromatolite columns (Fig. 5). In MSGa from both the apatite layer or interlayer space, the presence of nanoscopic inclusions of organic matter and carbonate (Fig. 9a-c) can have an origin influenced by microorganisms, and they possibly represent fossilized cells. Our data however do not unambiguously demonstrate that the MSGa are *bona fide* microfossils as they lack a distinct organic-wall, which is the primary criterion to recognize Precambrian microfossils in chert (Table 1 in Schopf et al., 2010). Organic cell walls of microfossils can be replaced by pyrite (including in phosphorites; see She et al., 2013), enclose framboidal pyrite cores or otherwise have intracellular structures of unknown composition (Schopf and Kudryavtsev, 2010; Wacey et al., 2012; Hofmann, 1976). If the MSGa are microfossils, this would be a different taphonomic style of preservation from the more classical carbonaceous microfossils in chert. If the MSGa are not microfossils, they could also possibly be micron-

1
2
3 547 size early diagenetic concretions, but there is no experimental or observational data to
4
5
6 548 support this. A speculative origin could be as nucleation and growth around nanoscale
7
8 549 particles of decayed and partly re-oxidised organic matter, but no concentric layers been
9
10 550 observed in the MSGA. This could be analogous to diagenetic dolomite micro-spheroids
11
12 551 observed in microbial mats from modern and recent sabkhas, although are these are
13
14
15 552 apparently more influenced by sulfate-reducing bacteria (Bontognali et al., 2010).
16
17

18 553 There are spatial and morphological similarities between the Badagaon MSGA (Fig.
19
20 554 2e-f, 6c-h) and the μm -size spheroidal objects interpreted as fossil bacteria reported from
21
22 555 Cenozoic East Australian phosphorites (O'Brien et al., 1980; 1981), Cenozoic Peruvian
23
24 556 phosphorites (Cosmidis et al., 2013b), Paleocene Moroccan phosphorites (Cosmidis et al.,
25
26 557 2013a), and Cretaceous stromatolitic phosphorites (Krajewski et al., 2000). In our samples
27
28 558 however, MSGA are preserved as discrete objects enveloped in an assemblage of silicified
29
30 559 calcite micro-spar itself embedded in later diagenetic dolomite cement (Fig. 13a). They do
31
32 560 not have an outer nanoscale layer of different crystallinity than the interior, which could
33
34 561 indicate a cellular membrane or wall.
35
36
37
38

39 562 We favor the microfossil interpretation of the MSGA in the Aravalli stromatolitic
40
41 563 phosphorites and further suggest that they are likely cyanobacterial in origin. Evidence for
42
43 564 growth-stage formation of nanoscale intracellular inclusions of carbonates has been
44
45 565 reported from stromatolite-building cyanobacteria (Couradeau et al., 2012), but also of
46
47 566 polyphosphate which can be the precursor to apatite (Benzerara et al., 2014). It is possible
48
49 567 that the Aravalli MSGA started permineralizing from cells in an organic ooze of EPS (Fig.
50
51 568 13b) during early diagenesis intermittently with periods of calcitisation. In this model,
52
53 569 collapsed nanoscale globules of organic matter and carbonate (such as those observed Fig.
54
55
56
57
58
59
60

9a-c) might be expected to remain trapped inside phosphatized microbial organic matter, hypothetically of the cellular fraction mixed with EPS. These nanoscopic inclusions of organic matter and carbonate could have formed during the internal collapse of cells saturated with Ca-phosphate, analogously to microbial phosphatization experiments (Benzerara et al., 2004a). However, MSGA-like structures observed in experiments with *Caulobacter* sp. have nanoscale layers of apatite with different crystallinity (Benzerara et al., 2004a), which have not been observed in Aravalli phosphorites. The presence of organic nano-inclusion in apatite shows that these phases preceeded the formation of the organic-free dolomite. However if indeed the MSGA are microfossils, then we would expect that this kind of phosphatisation would be preserved elsewhere.

In the Neoproterozoic Doushantuo phosphorites, the residual organic cell wall differs by being bounded by organic-filled cavities surrounded by nanoscale euhedral apatite crystals (She et al., 2013; 2014). It remains challenging however to identify the nature of microfossils solely on the basis of morphology as shown by the 'animal embryo' example from Neoproterozoic Doushantuo phosphorite. In fact, this exceptionally-preserved cellular material has been alternatively interpreted as fossil animal embryos (Xiao et al., 1998; Yin et al., 2007), as *Thiomargarita*-like sulphur bacteria (Bailey et al., 2007), as algae (Xue et al., 1999), and as encysting protists (Huldtgren et al., 2011). This important ongoing debate on the phylogenetic affinity of the Doushantuo 'animal embryos' well-illustrates the need for both detailed microscopy-based observations of taphonomically robust features (e.g. Xiao et al., 2007) and of using solid geochemical criteria at adequate scales. However, Doushantuo granular phosphorites contain abundant and diverse microfossils composed of N- and O-bearing organic matter (She et al., 2013).

1
2
3 593 These are generally entombed within apatite granules, which contain trace sulphate,
4
5
6 594 occasional diagenetic albite, and ambient inclusion trails, as well as later diagenetic rims of
7
8 595 isopachous apatite that sometimes has fine pyrite laminae (She et al., 2013). Many
9
10 596 microfossil morphologies are similar to modern cyanobacterial cells. While colonies of
11
12 597 *Myxococcoides* represent a third of all microfossil occurrences and dominate the
13
14 598 Doushantuo microfossil community, other common morphotypes include other spheroidal
15
16 599 to ellipsoidal unicells, septate and non-septate filaments, as well as coiled filaments that
17
18 600 cannot be easily assigned a phylogenetic affinity (She et al., 2014). These observations
19
20 601 have led to the suggestion that EPS produced by cyanobacteria-dominated microbial
21
22 602 communities form an ooze in highly productive shallow basins that adsorbs calcium and
23
24 603 phosphate to the point of supersaturation. Not only would this model provide a
25
26 604 straightforward means to trap nutrients and to bind nanoscale detrital particles, but it
27
28 605 could also be an underlying mechanism involved in the growth of stromatolites from
29
30 606 microbial mats and the preservation of microfossils as organo-apatite micro-spheroids.
31
32
33
34
35
36
37
38
39
40
41

42
43
44
45
46
47
48
49
50
51
52
53
54
55
56
57
58
59
60
5.3. On the formation of stromatolites

609 Cyanobacteria form only a minor proportion of the diverse array of microbes in
610 modern stromatolites (Burns et al., 2004; Papineau et al., 2005; Goh et al., 2009; Birgel et
611 al., 2015). The microbial community structure of the Aravalli stromatolitic phosphorite
612 could have included a benthic cyanobacterial component that accreted and biomineralised
613 apatite and calcite. Growth from microbial mats in stromatolite columns are represented
614 by protuberances of apatite coated in calcite, extending into what is now interlayer space,
615 filled with dolomite. These protuberances of microbial apatite extend from the layers of

1
2
3 616 apatite-calcite, which can be visualized as extensions of calcite and apatite from the main
4
5
6 617 layer of apatite in the microbial mat (Figs. 8c-d, 9d, 12f). This type of growth presumably
7
8 618 occurs towards sunlight and would favor the trapping and binding of environmental
9
10
11 619 particulates, which would have included pelagic cyanobacteria, mineral debris, and
12
13 620 decomposing organic matter. Modern stromatolites grown in the laboratory make bubbles
14
15 621 that have layers tens of microns in size linked by extensions a few microns long (e.g. Bosak
16
17
18 622 et al, 2013). In a refinement of the model of stromatolite growth and accretion, such
19
20 623 structures were hypothetically made of EPS and photosynthetic bacteria (Fig. 13b) and
21
22 624 they are analogous to the observations reported here.

23
24
25 625 Apatite rosettes sometimes have carbonate inclusions, as detected by micro-Raman
26
27 626 (e.g. arrows in Fig. 5e) or observed by SEM, which indicates that the initiation of
28
29
30 627 phosphatization co-occurred with calcitisation in the stromatolite columns. In the rosette
31
32 628 cores, the subsequent coat of silica permineralised around MSGA soon after their
33
34
35 629 phosphatisation. The presence of finely disseminated organic matter in the chert core (Fig.
36
37 630 5) of the apatite rosettes suggests that silicification occurred when organic matter was still
38
39
40 631 surrounding the phosphatizing microorganisms. It is not clear how soon after
41
42 632 sedimentation this happened, but the rosettes and their chert cores tend to preserve
43
44 633 similar relative size proportions, which suggests they formed during early diagenesis when
45
46 634 apatite was precipitating. Formation of hypothetical EPS-ooze would have been stimulated
47
48
49 635 by the periodic upwelling of deep phosphate-rich waters, which would have favored
50
51
52 636 biomineralisation in the mat, formation of EPS layers on top of biomineralised layers, and
53
54 637 trapping and binding by extensional protuberances.

55
56 638 The petrographic context of apatite rosettes in the intercolumnar space over areas
57
58
59
60

1
2
3
4
5
6
7
8
9
10
11
12
13
14
15
16
17
18
19
20
21
22
23
24
25
26
27
28
29
30
31
32
33
34
35
36
37
38
39
40
41
42
43
44
45
46
47
48
49
50
51
52
53
54
55
56
57
58
59
60

several millimeters wide along with fragments of microbial mats suggests that they formed at the time of sedimentation when a hypothetical EPS “cloud” was locally super-saturated with silica, perhaps stimulated directly by the presence of silicifying cyanobacteria (Fig. 13a). While apatite rosettes can form during early diagenesis experiments (Blake et al., 1998), apatite rosette occurring around chert cores have yet to be documented in experiments.

A common speculation about the composition and microstructures of the Aravalli stromatolitic phosphorites is that they are the result of *in situ* precipitation of calcium carbonate and its coeval and progressive ‘replacement’ by apatite (Chauhan, 1979). When supersaturation with respect to carbonate fluorapatite occurs in pore water solutions, calcium phosphate precipitation takes place (e.g. Benzerara et al., 2004a). The formation of dolomite in microbial mats is favored by the presence of sulphate (Vasconcelos et al., 2006; Bontognali et al., 2009) although there is no clear evidence for sulphate reducing microorganisms in the Aravalli phosphorites. The fact that MSGA constitute the layers of the apatite microbial mat with infillings of dolomite (Fig. 7f and 8d) combined with the presence of these objects in the protuberances and in the chert core of apatite rosettes point to a connection to cyanobacteria capable of silicification, calcification, and phosphatisation. This conclusion is also supported by the composition of organic matter, which was produced chiefly from N₂-fixing and CO₂-fixing cyanobacteria.

Since apatite layers in stromatolitic microbial mats are composed of MSGA, and organo-apatite rosettes in intercolumns contain MSGA in their chert cores, a common mechanism of phosphatization and calcification/silification is proposed. Based on independent confirmation of the mineralogy from EDS spectra by TEM, Ca2p XANES

spectra by STXM, and from elemental and molecular fragment analysis by ToF-SIMS, a sequence of events for the construction of the stromatolite environment is proposed in Fig. 13. The systematic occurrence of organic matter in apatite points to formation during early diagenesis in a calcium-phosphate saturated organic ooze (Fig. 13). The systematic occurrence of calcite associated with apatite, suggest in this context that calcitising microorganisms could have induced this early diagenetic biomineralisation followed by the subsequent crystallization of dolomite during later diagenetic residual Ca-Mg-carbonate and decomposed organic matter in pore solutions. Although apatite was abundant in the Aravalli environment, a similar sequence of biomineralization could likely be common for the formation and precipitation of stromatolites in other environments (e.g. Lepot et al., 2008; 2009). Micro-analytical approaches have been used to show that nanoscopic particles of organic matter are associated with early diagenetic sulphides in Neoarchean stromatolitic carbonates and thus preserve indigenous biosignatures of both bacterial sulphate reduction and the parent microorganisms that built and inhabited the stromatolite (Lepot et al., 2008; 2009).

5.4. Implications for the carbon cycle in the Aravalli Group

Carbon isotope fractionation during diagenesis and greenschist facies metamorphism can fractionate C isotopes and lead to ^{13}C -enriched residual organic matter of less than 4‰ (Desmarais, 2001), but the Raman spectra show that the organic matter has spectral characteristics consistent with greenschist facies metamorphism (red spectra in Fig. 5). While the organic matter in our samples is relatively crystalline graphitic carbon, it also preserves a range of molecular functional groups as well as nitrile. Organic matter

1
2
3
4
5
6
7
8
9
10
11
12
13
14
15
16
17
18
19
20
21
22
23
24
25
26
27
28
29
30
31
32
33
34
35
36
37
38
39
40
41
42
43
44
45
46
47
48
49
50
51
52
53
54
55
56
57
58
59
60

with ^{13}C -depleted compositions may also be attributable to a dominantly heterotrophic biomass (Eigenbrode and Freeman, 2006). The $\delta^{13}\text{C}_{\text{org}}$ values between -32.1 and -13.0‰ (Fig. 6) are also consistent with C-fixation with the pentose phosphate pathway and similar to previously reported values (Banerjee et al., 1986; Sreenivas et al., 2001; Papineau et al., 2013). Such ranges of $\delta^{13}\text{C}_{\text{org}}$ values have been proposed to be consistent with diffusion-limited CO_2 fixation, growth rates, and fluctuating CO_2 concentration (Laws et al., 1995). In the Neoproterozoic Chuar Group, variations in $\delta^{13}\text{C}_{\text{org}}$ values between -30 and -12‰ over a few meters of stratigraphy have been interpreted as evidence for eutrophication driven by high primary productivity (Nagy et al., 2009). In the Jhamarkotra embayment and other basins of the Lower Aravalli Group, evidence for high primary productivity has been suggested on the basis of organic-rich shales (Papineau et al., 2009), $\delta^{13}\text{C}_{\text{carb}}$ excursions in carbonate not associated with phosphorites (Papineau et al., 2013), and ^{13}C -enriched organic matter in carbonates, phosphorites and organic rich shales.

Based on the $\delta^{13}\text{C}_{\text{carb}}$ values of stromatolite columns at Jhamarkotra, which is ^{13}C -depleted by $1\text{--}2\text{‰}$ compared to intercolumnar carbonate (Fig. 6a), we suggest that diagenetic oxidation of organic matter contributed to column formation. In columns of stromatolitic phosphorite from the Udaipur Valley sulphide minerals rarely occur. Furthermore, $\delta^{13}\text{C}_{\text{org}}$ values of -12‰ along with columnar $\delta^{13}\text{C}_{\text{carb}}$ values as low as -2.8‰ are associated with low $\delta^{15}\text{N}_{\text{TN}}$ values, and TOC up to 3 wt\% (Fig. 6c-d). These compositions are distinct from typical marine sedimentary organic matter with $\delta^{13}\text{C}_{\text{org}}$ values around -24 to -27‰ and $\delta^{15}\text{N}$ values around $+5$ to $+7\text{‰}$ (Peters et al., 1978).

On the basis of these isotope compositions, cyanobacteria that fix CO_2 by RuBisCo likely dominated the stromatolitic phosphorite environment although other phototrophic

microorganisms could also have contributed to the measured $\delta^{13}\text{C}_{\text{org}}$ values. In fact, other CO_2 -fixation pathways can produce organic matter that is relatively enriched in ^{13}C , comparably to the fractionation of less than 10‰ imparted to initial CO_2 by several anoxygenic phototrophic bacteria (House et al., 2003) that included CO_2 -fixation using different forms of RuBisCo (e.g. *Rhodospseudomonas* sp.), the reductive TCA cycle (e.g. *Chlorobium* sp.), and the 3-hydroxipropionate pathway (e.g. *Chloroflexus* sp.).

Therefore the $\delta^{13}\text{C}$ for the Badagaon stromatolitic phosphorites point to 1) aerobic heterotrophy during early diagenesis that produced the isotopically light carbonate and indirectly the later diagenetic dolomite cement, and 2) CO_2 -fixing cyanobacteria using the pentose phosphate pathway and RuBisCo populated the microbial mats of the stromatolite columns and thrived in phosphate-rich but sulphate- and Fe-poor waters. Heterotrophs in Aravalli stromatolitic phosphorites likely included photoheterotrophic bacteria and might have included methanotrophs as suggested by a single $\delta^{13}\text{C}$ analysis at -39.4‰ (Table 3). However, the near absence of sulphides and the absence of organic sulphur from the C-XANES and ToF-SIMS spectra (as $^{32}\text{S}^-$) is inconsistent with a significant role for anaerobic microorganisms.

The organic geochemistry of carbon in stromatolitic phosphorites is an important consideration in our interpretations and model. Olefinic, aromatic C=C, and alcohol functional groups were detected in organic matter from stromatolitic phosphorites from both Jhamarkotra and Badagaon (Fig. 10). Such molecular residues are commonly associated with decayed biomass (Bernard et al. 2009; De Gregorio et al. 2009, 2011). In a few samples, these heteroatomic peaks are quite intense (Figs. 10, 11), and are usually accompanied by distinct, sharp nitrile and/or amidyl peaks in corresponding N-XANES

1
2
3 731 spectra, even while the π^* and σ^* C-XANES peaks for aromatic carbon (at 285.3 eV and
4
5 732 291.7 eV, respectively) imply a significant degree of graphitization. An abundance of C=O
6
7
8 733 and C-O functionality in organic matter from phosphorites is consistent with a possible
9
10 734 origin from EPS, rich in O-bearing polysaccharides (Boyce et al. 2002; Lawrence et al.
11
12
13 735 2003).

14
15 736 All these observations support our diagenetic model for organic matter from
16
17 737 cyanobacteria-dominated biomass in shallow-marine environments. The low C:N_{AT} ratios
18
19 738 of intercolumns of stromatolitic phosphorites contrasts with diagenetically-processed
20
21 739 organic matter in black shales with variable and high C:N_{AT} and C:P_{AT} (Fig. 5f-i - Papineau et
22
23 740 al., 2009). However, the organic matter from both the shallow-marine environments
24
25 741 (represented by stromatolites) and the deep marine environments (represented by black
26
27 742 shales) has geochemical composition consistent with biomass originally produced by
28
29 743 primary producers, but subsequently variably altered. Sub-oxic to anoxic (but not
30
31 744 sulphidic) nutrient-rich bottom waters was likely regenerated from the organic-rich
32
33 745 sediments of the black shales in Udaipur Valley (Papineau et al., 2009; 2013).
34
35
36
37
38
39
40
41

42 747 **5.5. Implications for the nitrogen cycle in the Phosphate Domain**

43
44 748 Organic-rich shales from the Udaipur basin accumulated in deep water environment
45
46 749 and have high $\delta^{15}\text{N}_{\text{TN}}$ values up to +28‰ as well as generally high C:N_{AT} above 50, are
47
48 750 interpreted to indicate a redox-stratified microbial ecosystem with high levels of secondary
49
50 751 productivity and the activity of microbial ammonium assimilation (Papineau et al., 2009).
51
52 752 The elevated content of organic matter in the carbonaceous shales from nearby in Amberi
53
54
55 753 (up to 14%wt) combined with their narrow range of $\delta^{13}\text{C}_{\text{org}}$ values near -29‰ suggests
56
57
58
59
60

that intense primary productivity fueled intense secondary productivity in a chemically-layered water column. This is also supported by the systematically high C:P ratios in Amberi shales (up to 13250; Papineau et al., 2013). The photic zone of such deep water environments would have been populated by an active microbial community. The phototrophic communities in the photic zone and near the oxygen minimum zone were actively biomineralizing apatite and calcite.

With metamorphic grade at the greenschist facies, such low $\delta^{15}\text{N}_{\text{TN}}$ values represent maximum values of pre-metamorphic nitrogen (Thomazo and Papineau, 2013 and references therein). Greenschist facies metamorphism can lead to N losses and ^{15}N -enrichments of residual N by a few ‰ (Bebout and Fogel, 1992; Bebout, 1997; Mingram and Brauer, 2001; Haendel et al., 1986; Boyd, 2001a; 2001b; Boyd and Philippot, 1998). Nitrogen isotope fractionation during growth experiments on different diazotrophic bacteria have shown that the Mo-nitrogenase yields biomass with $\delta^{15}\text{N}$ value down to about -2‰, which is less fractionated than when Fe- or V-nitrogenase is used (Zerkle et al., 2008; Zhang et al., 2014). Badagaon stromatolitic phosphorites have $\delta^{15}\text{N}$ values of -1.2 to +2.7‰, which is most consistent with diazotrophs using the Mo-nitrogenase followed by small fractionation from metamorphic N loss. Likewise, the systematically light nitrogen isotope compositions are inconsistent with a large population of denitrifying microbes and rather point to fractionation by nitrogen-fixing organisms (Fig. 5b) (Macko et al., 1987). Our interpretation is also inconsistent with previously proposed qualitative models of phosphogenesis mediated by high rates of denitrification (Piper and Cadispori, 1975). Most of the measured light $\delta^{15}\text{N}_{\text{TN}}$ values were detected in intercolumnar space (Table 3), which suggest that N may be better preserved in these areas. It is possible that in the

1
2
3
4
5
6
7
8
9
10
11
12
13
14
15
16
17
18
19
20
21
22
23
24
25
26
27
28
29
30
31
32
33
34
35
36
37
38
39
40
41
42
43
44
45
46
47
48
49
50
51
52
53
54
55
56
57
58
59
60

777 stromatolitic phosphorites from the Jhamarkotra embayment, the inferred past presence of
778 Fe-oxidizing filamentous bacteria (Crosby et al., 2014) was accompanied by decomposition,
779 since no N was detected from Jhamarkotra stromatolitic phosphorites.

780 The crystallinity and composition of organic matter in stromatolitic phosphorites is
781 similar to that preserved in black shales from the PD, except for N molecular functional
782 groups (Fig. 10 and 11; Table 2), which demonstrates that the N is syngenetic. The
783 presence of compositionally distinct molecular functional groups suggest that there were
784 different microbial communities in these distinct environments, especially those associated
785 with organic decomposition. Intercolumnar dolomite contains organic matter with C:N_{AT}
786 ratios typically less than 3.5 (only one data, from a stromatolite column with C:N_{AT} = 8.2)
787 and, because the Redfield C:N_{AT} ratio of modern (and most likely ancient) planktonic
788 biomass is typically around 4-10, nitrogen loss due to metamorphism was evidently
789 limited. Therefore N isotope compositions are only minimally affected by post-
790 depositional processes. The systematically low C:N_{AT} and $\delta^{15}\text{N}_{\text{TN}}$ values in Badagaon and
791 other localities of the Udaipur Valley (including Kanpur and Dakankotra) are consistent
792 with biological N fixation during deposition. Negative $\delta^{15}\text{N}$ analyses are interpreted to have
793 arisen from biological N₂ fixation as this is consistent with experiments (Minagawa and
794 Wada, 1986; Macko et al., 1987).

795 XANES spectra at the N1s edge from microtomed organic matter have several peaks
796 that represent different N-bearing molecular functional groups. The 399.8 eV peak
797 represents nitrile functional groups (Shard et al., 2004; Leinweber et al., 2007) or pyridine
798 (Valiravamurthy and Wang, 2002). Also detected were peaks of or amidyl and/or peptidyl
799 groups at 400.9 to 401.1 eV (Cody et al., 2011) and nitro-groups at 403.7 eV, 404.5-405.0

1
2
3 800 eV, and 530.8 eV (Leinweber et al., 2007; Cody et al, 2011 – Figs. 10 and 11). While only the
4
5
6 801 404.5-405.0 eV peaks were observed in acid-insoluble organic matter from Badagaon
7
8 802 stromatolitic phosphorites, peaks for all the above nitro-groups have been observed in
9
10 803 organic matter from black shales (Figs. 10 and 11). In particular, the co-occurrence of
11
12 804 nitrile and carboxylic acid (288.4 eV) in organic matter extracted from two black shale
13
14 805 samples from the PD (DD-1 and UV0609) is similar but less intense in the NPD shales (Fig.
15
16 806 11a). At the N-edge, nitrile was detected in organic matter from black shales from the
17
18 807 Udaipur Valley and in one stromatolitic phosphorite sample from Jhamarkotra (Fig. 10).
19
20 808 Nitro- groups were also possibly detected at 404.5 eV, but these unresolved peaks occur at
21
22 809 the maximum peak intensity of N edge. Unfortunately, because these spectra were
23
24 810 acquired over different analytical sessions for this work, we cannot independently confirm
25
26 811 the C:N_{AT} of Aravalli organic matter by STXM. Aliphatic carbon at 287.3 eV was resolved in
27
28 812 black shale sample AB-3 and possibly (at 286.6 eV) in the stromatolitic phosphorite from
29
30 813 Jhamarkotra (JK0606; Fig. 10).
31
32
33
34
35
36

37 814 Nitrile bonds should be among the most geologically stable N bonds with C and
38
39 815 relevant for the rock record. The 399.8 eV peaks indicate an organic origin for the N and
40
41 816 $\delta^{15}\text{N}$ compositions analysed independently in this study. Deamination and transamination
42
43 817 reactions during diagenesis lead to direct loss of nitrogen (Boyd, 2001b), whereas
44
45 818 dehydrogenation and dehydration reactions of residual amino groups during
46
47 819 metamorphism could be responsible for the observed organic N preserved as nitrile
48
49 820 functional groups (Fig. 7). The cause of the distinct occurrences of N-poor phosphorites
50
51 821 from the Jhamarkotra Formation is unclear but might be due to a different kind of organic
52
53
54
55
56
57
58
59
60

1
2
3 822 decomposition in the Jhamarkotra embayment or possibly relate to a different style of
4
5
6 823 organic preservation.

7
8 824 Another notable molecular fragment of the CN- peak detected in the ToF-SIMS
9
10 825 spectrum from the nano-fabricated lamella (Fig. 12a) is unlikely to be from contamination
11
12 826 and was possibly resolved in the C-XANES spectrum at 288.5eV (Fig. 10). Possible sources
13
14
15 827 of contaminant in this spectrum include carbonyl from the W(CO₃)₆ welding vapor used for
16
17
18 828 nano-fabrication, residual hydrocarbon volatiles deposited during prior electron beam
19
20 829 imaging in the FIB and/or TEM sample chambers, hydrocarbon volatiles adsorbed from air
21
22
23 830 between analyses. The first possible contaminant would presumably yield oxidized
24
25 831 carbonate on the sample as opposed to hydrocarbons or N compounds. Finally, volatile
26
27
28 832 hydrocarbons are unlikely as we used an Evactron system in the FIB and pre-sputtering
29
30 833 prior to ToF-SIMS analyses. Unfortunately, there are no comparable ToF-SIMS analyses of
31
32 834 FIB lamellae, but clearly this independent confirmation of organic nitrogen is a promising
33
34
35 835 result for these combined techniques.

36
37 836
38
39 837 **6. Conclusions**

40
41
42 838 Nanoscale petrographic and geochemical features of phosphatized microbial
43
44 839 communities are preserved in Paleoproterozoic stromatolitic phosphorites, and are used
45
46
47 840 here to propose a new model for the formation of stromatolitic phosphorites (Fig. 13). We
48
49 841 describe mineral associations from a microbial mat inside a stromatolite column composed
50
51 842 of alternating layers of apatite and calcite. New Raman, EDS, and C-and Ca-XANES data
52
53
54 843 show that MSGA occur in layers and interlayers of stromatolitic microbial mats and also
55
56 844 inside the chert core of diagenetic apatite rosettes in between columns. In the
57
58
59
60

intercolumnar space of the stromatolitic phosphorite from Badagaon, MSGA occur in apatite rosettes that share similarity to siderite rosettes from diagenetic experiments (Koehler et al., 2013) and to apatite rosettes from phosphatisation experiments (Blake et al., 1998) as well as other examples from Precambrian jaspiliic banded iron formations (Heaney and Veblen, 1990) and organic-rich cherts (Mossman et al., 2005). The Badagaon apatite rosettes are more likely of diagenetic origin rather than bona fide microfossils as previously suggested (Chauhan, 1979; *cf.* Kazmierczak, 1979).

In the microbial mat, MSGA are systematically associated with calcite micro-spar. Stromatolite accretion and phototrophic growth is proposed to have involved micron-size protuberances extending into mat interlayers from the stromatolitic microbial mat composed of MSGA coated in calcite micro-spar. Apatite in mat layers is also peppered by nanoscopic inclusions of organic matter and carbonate. A possible explanation for nanoscale organic particles in apatite is that the finely disseminated organic matter represents an organic mixture that originated from EPS, which would have CO-rich molecular functional groups due to high levels of initial polysaccharides. Blooming cyanobacteria would have become entombed in carbonate-fluorapatite when calcium-phosphate-carbonate reached super-saturation preceding dehydration. The new nanoscale petrological data of apatite, chert, and calcite can be used to suggest formation during the early diagenetic (bio-?) mineralisation processes of phosphatisation, calcitisation, and silicification.

While She et al. (2013, 2014) found compelling evidence for the presence of cyanobacteria in shallow-marine granular phosphorites from the Doushantuo Fm., others have emphasized the presence and role of other microorganisms involved in S and C cycles

1
2
3
4
5
6
7
8
9
10
11
12
13
14
15
16
17
18
19
20
21
22
23
24
25
26
27
28
29
30
31
32
33
34
35
36
37
38
39
40
41
42
43
44
45
46
47
48
49
50
51
52
53
54
55
56
57
58
59
60

of phosphogenic environments. For instance, giant sulphur bacteria have been inferred in Doushantuo phosphorites (Bailey et al., 2007), filamentous iron-oxidizing bacteria from phosphorites in Jhamarkotra (Crosby et al. 2014), sulphur-oxidizing bacteria from modern phosphatic mud near the coast of Namibia (Schultz and Schultz, 2005), coupled methanotrophic and sulphur-oxidizing bacteria in Zaonega concretionary phosphatic organic-rich mudstones (Lepland et al., 2013), and finally coupled sulphate and iron reducing bacteria in Michigamme granular phosphorites (Hiatt et al., 2015). Indeed the availability of Fe and Mn might relate to the presence of Fe-oxidizing bacteria or an active redox shuttle with metal-oxide bound apatite (Pufahl and Hiatt, 2012; Follmi, 1996).

The diversity of such possible microorganisms in phosphorites may be due to the relative depth at which the phosphorites form and thus may relate to the dominant microorganisms in some communities. While it is possible that the variability in $\delta^{13}\text{C}_{\text{org}}$ values may be attributable to the presence of biomass with microorganisms capable of CO_2 fixation using the reductive TCA cycle, 3-hydroxipropionate pathway (House et al., 2003), the most likely dominant pathway for fractionation of the $\delta^{13}\text{C}_{\text{org}}$ composition of stromatolitic phosphorites in Aravalli is through the pentose phosphate pathway. The presence of isotopically light N in the Badagaon phosphorites points to biological N_2 -fixation. While N fixation can be performed by methanogens (Boyd et al., 2009), the bulk of our $\delta^{13}\text{C}_{\text{org}}$ values (except a single $\delta^{13}\text{C}_{\text{org}}$ value at -39.4‰) is most consistent with carbon fixation by the pentose phosphate pathway. A similar range of $\delta^{13}\text{C}_{\text{org}}$ values measured in situ on cyanobacteria-like Proterozoic microfossils have been interpreted similarly (Williford et al., 2013). This does not exclude possible contributions from some phototrophic Fe(II)-oxidizing bacteria (Crosby et al., 2014), which are known to live in the

photic zone of modern rift lakes (Crowe et al., 2008). There is also the likely possibility that anoxygenic phototrophic microorganisms participated in the formation of these stromatolites, as they have been reported from modern stromatolites (Papineau et al., 2005; Goh et al., 2009; Bosak et al., 2009; Birgel et al., 2015).

We conclude here cyanobacteria played a central role in the biomineralisation of apatite, calcite and chert at Badagaon and were thus key in the formation of the Aravalli stromatolitic phosphorites.. Our results point to a new formation model of shallow-marine Aravalli stromatolitic phosphorites, where 1) the carbon isotope is consistent with fractionation by the RuBisCo enzyme 2) nitrogen isotope data can be shown to be an organic biosignature, which here points to the dominance of biological N₂ fixation, 3) microscopic spheroidal grains of apatite might represent phosphatised cyanobacterial cells in calcitised or silicified extracellular polymeric substances, 4) later dolomitisation in stromatolite columns occurred in part from re-oxidised organic matter, 5) promising ToF-SIMS analysis of FIB lamella allow microscopic sedimentary structures to be spatially resolved, such as protuberances extending from microbial mats, as well as the detection of CN⁻, and independent confirmation of molecular functional groups detected by STXM, and 6) the excellent preservation of the organic matter can be qualitatively confirmed by Raman spectra and organic molecular composition with nitrile, carboxylic acid, alcohol, and aliphatic hydrocarbons. These biosignatures from Badagaon stromatolitic phosphorites point to the importance of cyanobacteria in shallow-marine phosphorites and to metabolically distinct microorganisms involved in the C, N, S, and Fe cycles in different phosphorites as likely related to the water column depth and the location of the oxygen minimum zone. The local abundance of oxidants, such as sulphate, which might influence

1
2
3
4
5
6
7
8
9
10
11
12
13
14
15
16
17
18
19
20
21
22
23
24
25
26
27
28
29
30
31
32
33
34
35
36
37
38
39
40
41
42
43
44
45
46
47
48
49
50
51
52
53
54
55
56
57
58
59
60

the preservation of sulphides. In the updated Paleoproterozoic scenario proposed here, phosphatisation of stromatolites would have been permitted only after O₂ levels had increased sufficiently for organic degradation to occur and upwelling-induced phosphatisation to stimulate cyanobacteria to biomineralise apatite, chert, and calcite.

Acknowledgements:

Correspondence

References

Alexander, C.M.O'D., Fogel, M., Yabuta, H., and Cody, G.D. (2007) The origin and evolution of chondrites recorded in the elemental and isotopic compositions of their macromolecular organic matter. *Geochim. Cosmochim. Acta* **71**, 4380–4403.

Apen, E., Hitchcock, A.P., and Gland, J.L. (1993) Experimental studies of the core excitation of imidazole, 4, 5-dicyanoimidazole, and s-triazine. *J. Phys. Chem.* **97**, 6859–6866

Banerjee, D.M., Schidlowski, M. and Ameth, J.D. (1986) Genesis of upper Proterozoic-Cambrian phosphorite deposits of India: Isotopic inferences from carbonate fluoapatite, carbonate and organic carbon. *Precambrian Research* **33**, 239-253.

Banerjee, D. M., Basu, P.C., Srivastava, N. (1980) Petrology, mineralogy, geochemistry, and origin of the Precambrian Aravallian phosphorite deposits of Udaipur and Jhabua, India. *Economic Geology* **75**, 1181-1199.

- 936 Banerjee, D.M. (1971) Precambrian stromatolitic phosphorites of Udaipur, Rajasthan, India,
937 *Geol. Soc. Am. Bull.* **82**, 2319-2329.
- 938 Battison, L. and Brasier, M.D. (2012) Remarkably preserved prokaryote and eukaryote
939 microfossils within 1Ga-old lake phosphates of the Torridon Group, NW Scotland.
940 *Precambrian Research* **196–197**, 204-217.
- 941 Bailey, J.V., Joye, S.B., Kalanetra, K.M., Flood, B.E. and Corsetti, F.A. (2007) Evidence of giant
942 sulphur bacteria in Neoproterozoic phosphorites. *Nature* **445**, 198-201.
- 943 Bebout, G.E. and Fogel, M.L. (1992) Nitrogen-isotope compositions of metasedimentary rocks
944 in the Catalina Schist, California: Implications for metamorphic devolatilization history.
945 *Geochim. Cosmochim. Acta* **56**, 2839-2849.
- 946 Bebout, G. E. (1997) Nitrogen isotope tracers of high-temperature fluid-rock interactions: Case
947 study of the Catalina Schist, California. *Earth Planet. Sci. Lett.* **151**, 77-90.
- 948 Benzerara, K., Menguy, N., Guyot, F., Skouri, F., de Luca, G., Barakat, M., and Heulin, T.
949 (2004a) Biologically controlled precipitation of calcium phosphate by *Ramlibacter*
950 *tatouinensis*. *Earth and Planetary Science Letters* **228**, 439-449.
- 951 Benzerara, K., Yoon, T.H., Tylicszak, T., Constantz, B., Spormann, A. M., and Brown, G.E.
952 (2004b) Scanning transmission X-ray microscopy study of microbial calcification,
953 *Geobiology* **2**, 249-259.
- 954 Benzerrara, K., Skouri-Panet, F., Li, Ferard, C., Gugger, M., Laurent, T., Couradeau, E., Ragon,
955 M., Cosmidis, J., Menguy, N., Margaret-Oliver, I., Tavera, R., Lopez-Garcia, P., and
956 Moreira, D. (2014) Intracellular Ca-carbonate biomineralization is widespread in
957 cyanobacteria. *P.N.A.S.* **111**, 10933-10938.
- 958 Bertrand-Sarfati, J., Flicoteaux, R., Moussine-Pouchkine, A., and Ahmed, A.A.K. (1997) Lower

- 959 Cambrian apatitic stromatolites and phosphoarenites related to the glacio-eustatic
960 cratonic rebound (Sahara, Algeria). *Journal of Sedimentary Research* **67**, 957-974.
- 961 Bernard, S., Benzerara, K., Beyssac, O., Brown, G.E., Grauvogel Stamm, L., and Düringer, P.
962 (2009) Ultrastructural and chemical study of modern and fossil sporoderms by
963 Scanning Transmission X-ray Microscopy (STXM). *Rev. Palaeobotany and palynology*
964 **156**, 248-261.
- 965 Bernard, S., Beyssac, O. and Benzerara, K. (2008) Raman mapping using advanced line-
966 scanning systems: geological applications. *Applied spectroscopy* **62**, 1180-1188.
- 967 Bernard, S., Wirth, R., Schreiber, A., Schulz, H.-M., and Horsfield, B. (2012) Formation of
968 nanoporous pyrobitumen residues during maturation of the Barnett Shale (Fort Worth
969 Basin). *International Journal of Coal Geology* **103**, 3-11.
- 970 Beyssac, O., Goffé, B., Chopin, C. and Rouzaud, J.N. (2002) Raman spectra of carbonaceous
971 material in metasediments: a new geothermometer. *Journal of metamorphic Geology* **20**,
972 859-871.
- 973 Birgel, D., Meister, P., Lundberg, R., Horath, T.D., Bontognali, T.R.R., Bahniuk, A.M., De
974 Rezende, C.E., Vasconcelos, C., and McKenzie, J.A. (2015) Methanogenesis produces
975 strong ^{13}C enrichment in stromatolites of Lagoa Salgada, Brazil: a modern analogue
976 for Palaeo-/Neoproterozoic stromatolites? *Geobiology* DOI: 10.1111/gbi.12130, 1-
977 22.
- 978 Blake, R.E., O'Neil, J.R., and Gracia, G.A (1998) Effects of microbial activity on the $\delta^{18}\text{O}$ of
979 dissolved inorganic phosphate and textural features of synthetic apatites. *American*
980 *Mineralogist* **83**, 1516-1531.
- 981 Bontognali, T.R.R., Vasconcelos, C., Warthmann, R.J., Bernasconi, S.M., Dupraz, C.,

- 1
2
3 982 Strohmenger, C.J., and McKenzie, J.A. (2010) Dolomite formation within microbial
4
5 983 mats in the coastal sabkha of Abu Dhabi. *Sedimentology* **57**, 824-844.
6
7
8 984 Bosak, T., Greene, S.E., and Newman, D.K. (2007) A likely role for anoxygenic photosynthetic
9
10 985 microbes in the formation of ancient stromatolites. *Geobiology* **5**, 119-126.
11
12 986 Boyce, C.K., Cody, G.D., Feser, M. (2002) Organic chemical differentiation within fossil plant
13
14 987 cell walls detected with X-ray spectromicroscopy. *Geology* **30**, 1039–1042.
15
16
17 988 Boyd, E.S., Anbar, A.D., Miller, S., Hamilton, T.L., Lavin, M., and Peters, J.W. (2009) A late
18
19 989 methanogen origin for molybdenum-dependent nitrogenase. *Geobiology* **9**, 221-232.
20
21 990 Boyd, S. R. (2001a) Nitrogen in future biosphere studies. *Chem. Geol.* **176**, 1-30.
22
23 991 Boyd, S. R. (2001b) Ammonium as a biomarker in Precambrian metasediments. *Precamb. Res.*
24
25 992 **108**, 159-173.
26
27 993 Boyd, S. R. and Philippot, P. (1998) Precambrian ammonium biogeochemistry: A study of the
28
29 994 Moine metasediments, Scotland. *Chem. Geol.* **144**, 257-268.
30
31
32 995 Burns, B.P., Goh, F., Allen, M., and Neilan, B.A. (2004). Microbial diversity of extant
33
34 996 stromatolites in the hypersaline marine environment of Shark Bay, Australia. *Environ*
35
36 997 *Microbiol* **6**, 1096–1101.
37
38
39 998 Bushinskii, G.I. (1966) The origin of marine phosphorites. *Lithology and Mineral Resources* **3**,
40
41 999 292–311.
42
43
44 1000 Cameron, E.M. (1983) Evidence from early Proterozoic anhydrite for sulphur isotopic partitioning
45
46 1001 in Precambrian oceans. *Nature* **304**, 54-56.
47
48
49 1002 Carter, C.B. and Kohlstedt, D.L. (1981) Electron irradiation damage in natural quartz grains.
50
51 1003 *Physics and Chemistry of Minerals* **7**, 110-116.
52
53
54 1004 Canfield, D.E. (1998) A new model for Proterozoic ocean chemistry, *Nature* **396**, 450-453.
55
56
57
58
59
60

1
2
3 1005 Chauhan, D.S. (1979) Phosphate-bearing stromatolites of the Precambrian Aravalli phosphorite
4
5
6 1006 deposits of the Udaipur region, their environmental significance and genesis of
7
8 1007 phosphorite. *Precambrian Res.* **8**, 95-126.
9
10
11 1008 Cody, G.D., Botto, R.E., Ade, H., and Wirick, S. (1996) The application of soft X-ray
12
13 1009 microscopy to the in-situ analysis of sporinite in coal. *International Journal of Coal*
14
15 1010 *Geology* **32**, 69-86.
16
17
18 1011 Cody, G.D., Alexander, C.M.O'D., Yabuta, H., Kilcoyne, A.L.D. Araki, T., Ade, H., Dera, P. Fogel,
19
20 1012 M., Militzer, B., and Mysen, B.O. (2008) Organic thermometry for chondritic parent
21
22 1013 bodies. *Earth and Planetary Science Letters* **272**, 446-455.
23
24
25 1014 Cody, G.D., Heying, E., Alexander, C.M.O'D., Nittler, L.R., Kilcoyne, A.L.D., Sandford, S.A., and
26
27 1015 Stroud, R.M. (2011) Establishing a molecular relationship between chondritic and
28
29 1016 cometary organic solids. *Proceedings of the National Academy of Sciences* **108**,
30
31 1017 19171-19176.
32
33
34 1018 Condie K.C., DesMarais, D.J., and Abbott, D. (2001) Precambrian superplumes and
35
36 1019 supercontinents: a record in black shales, carbon isotopes, and paleoclimates?
37
38 1020 *Precambrian Research* **106**, 239-260.
39
40
41 1021 Cook, P.J. and Shergold, J.H. (1984) Phosphorus, phosphorites and skeletal evolution at the
42
43 1022 Precambrian-Cambrian boundary. *Nature* **308**, 231-236.
44
45
46 1023 Cosmidis, J., Benzerara, K., Gheerbrant, E., Estève, I., Bouya, B., Amaghazaz, M., (2013a)
47
48 1024 Nanometer-scale characterization of exceptionally preserved bacterial fossils in
49
50 1025 Paleocene phosphorites from Ouled Abdoun (Morocco). *Geobiology* **11**, 139-153.
51
52
53 1026 Cosmidis, J., Benzerara, K., Menguy, N., and Arning, E. (2013b) Microscopy evidence of
54
55 1027 bacterial microfossils in phosphorite crusts of the Peruvina shelf: Implications for
56
57
58
59
60

- 1028 phosphogenesis mechanisms. *Chemical Geology* **359**, 10-22.
- 1029 Couradeau, E., Benzerara, K., Gérard, E., Moreira, D., Bernard, S., Brown, G.E., López-García,
1030 P. (2012) An early-branching microbialite cyanobacterium forms intracellular carbonates.
1031 *Science* **336**, 459-462.
- 1032 Crosby, C.H., Bailey, J., and Sharma, M. (2014) Fossil evidence of iron-oxidizing
1033 chemolithotrophy linked to phosphogenesis in the wake of the Great Oxidation
1034 Event. *Geology* **42**, 1015-1018.
- 1035 Crowe, S.A., Jones, C.A., Katsev, S., Magen, C., O'Neill, A.H., Sturn, A., Canfield, D.E., Haffner,
1036 G.D., Mucci, A., Sundby, B., Fole, D.A. (2008) Photoferrotrophs thrive in an Archean
1037 Ocean analogue. *Proceedings of the National Academy of Sciences of the U.S.A.* **105**,
1038 15938-15943.
- 1039 De Gregorio, B.T., Sharp, T.G., Flynn, G.J., Wirick, S., and Hervig, R.L. (2009) A biogenic origin
1040 for Earth's oldest putative microfossils. *Geology* **37**, 631-634.
- 1041 De Gregorio, B.T., Sharp, T.G., Rushdi, A.I., and Simoneit, B.R.T. (2011) Bugs or gunk?
1042 Nanoscale methods for assessing the biogenicity of ancient microfossils and organic
1043 matter. In: Golding, S.D., Glikson, M. (Eds.), *Earliest Life on Earth: Habitats,*
1044 *Environments, and Methods of Detection*, Springer, Dordrecht, Netherlands, 239-289.
- 1045 Desmarais, D. (2001) Isotopic evolution of the biogeochemical carbon cycle during the
1046 Precambrian. *Reviews in Mineralogy and Geochemistry* **43**, 555-578.
- 1047 Dhez, O., Ade, H., and Urquhart, S.G. (2003) Calibrated NEXAFS spectra of some common
1048 polymers. *J. Electron Spectrosc. Relat. Phenom.* **128**, 85-96.
- 1049 Eigenbrode, J.L. and Freeman, K.H. (2006) Late Archean rise of aerobic microbial
1050 ecosystems. *Proc. Natl. Acad. Sci. U.S.A.* **103**, 15759-15764.

1
2
3 1051 Follmi, K.B. (1996) The phosphorus cycle, phosphogenesis and marine phosphate-rich deposits.
4
5
6 1052 *Earth Science Reviews* **40**, 55-124.
7
8 1053 Goh, F., Allen, M.A., Leuko, S., Kawaguchi, T., Decho, A.W., Burns, B.P., and Neilan, B.A.
9
10 1054 (2009) Determining the specific microbial populations and their spatial distribution
11
12 1055 within the stromatolite ecosystem of Shark Bay. *The ISME Journal* **3**, 383-396.
13
14
15 1056 Habicht, K.S., Gade, M., Thamdrup, B., Berg, P., and Canfield, D.E. (2002) Calibration of
16
17 1057 sulfate levels in the Archean ocean. *Science* **298**, 2372-2374.
18
19
20 1058 Haendel, D., Mühle, K., Nitzsche, H.-M., Stiehl, G., and Wand, U. (1986) Isotopic variations of
21
22 1059 the fixed nitrogen in metamorphic rocks. *Geochim. Cosmochim. Acta* **50**, 749-758.
23
24
25 1060 Heaney, P.J. and Veblen, D.R. (1990) An examination of spherulitic dubiomicrofossils in
26
27 1061 Precambrian banded iron formations using the transmission electron microscope.
28
29 1062 *Precambrian Research* **49**, 355-372.
30
31
32 1063 Hiatt, E.E., Pufahl, P.K., and Edwards, C.T. (2015) Sedimentary and associated fossil bacteria in
33
34 1064 a Paleoproterozoic tidal flat in the 1.85 Ga Michigamme Formation, Michigan, USA.
35
36 1065 *Sedimentary Geology* **319**, 24-39.
37
38
39 1066 Hofmann, H.J. (1976) Precambrian microflora, Belcher Islands, Canada: significance and
40
41 1067 systematics. *Journal of Paleontology* **50**, 1040-1073.
42
43
44 1068 Hultgren, T., Cunningham, J.A., Yin, C., Stampanoni, M., Marone, F., Donoghue, P.C.J. and
45
46 1069 Bengtson S. (2011) Fossilized Nuclei and Germination Structures Identify Ediacaran
47
48 1070 “Animal Embryos” as Encysting Protists. *Science* **334**, 1696-1699.
49
50
51 1071 Ishii, I., and Hitchcock, A.P. (1988) The oscillator strengths for C1s and O1s excitation of some
52
53 1072 saturated and unsaturated organic alcohols, acids, and esters. *Journal of Electron*
54
55 1073 *Spectroscopy and Related Phenomena* **46**, 55-84.
56
57
58
59
60

- 1074 Kaufman, A.J. and Knoll, A.H. (1995) Neoproterozoic variations in the C-isotopic composition
1075 of seawater: stratigraphic and biogeochemical implications. *Precambrian Research* **73**,
1076 27–49.
- 1077 Kazmierczak, J. (1979) The Eukaryotic nature of Eosphaera-like ferriferou structures from the
1078 Precambrian Gunflint iron formation, Canada: A comparative study. *Precambrian*
1079 *Research* **9**, 1-22.
- 1080 Kikuma, J., Warwick, T., Shin, H.-J., Zhang, J., and Tonner, B.P. (1998) Chemical state analysis
1081 of heat-treated polyacrylonitrile fiber using soft X-ray spectromicroscopy. *Journal of*
1082 *Electron Spectroscopy and Related Phenomena* **94**, 271-278.
- 1083 Kilcoyne, A. L. D., Tyliszczak, T., Steele, W. F., Fakra, S., Hitchcock, P., Franck, K., Anderson,
1084 E., Harteneck, B., Rightor, E. G., Mitchell, G. E., Hitchcock, A. P., Yang, L., Warwick, T.,
1085 Ade, H. (2003). Interferometer-controlled scanning transmission X-ray microscopes
1086 at the Advanced Light Source, *The Journal of Synchrotron Radiation* **10**, 125-136.
- 1087 Köhler, I., Konhauser, K.O., Papineau, D., Bekker, A., and Kappler, A. (2013) Biological carbon
1088 precursor to diagenetic siderite spherulites in banded iron formations. *Nature*
1089 *Communication* **4**:1741, 1-7.
- 1090 Krajewski, K.P., Lesniak, P.M. Lacka, B., and Zawidzki (2000) Origin of phohpatic
1091 stromatolites in the Upper Cretaceous condensed sequenc of the Polish Jura chain.
1092 *Sedimentary Geology* **136**, 89-112.
- 1093 Lawrence, J.R., Swerhone, G.D.W., Leppard, G.G., Araki, T., Zhang, X., West, M.M., and
1094 Hitchcock, A.P. (2003) Scanning transmission X-ray, laser scanning, and transmission
1095 electron microscopy mapping of the exopolymeric matrix of microbial biofilms. *Applied*
1096 *and Environmental Microbiology* **69**, 5543-5554.

- 1097 Laws, E.A., Popp, B.N., Bidigare, R.R., Kennicutt, M.C., and Macko, S.A (1995) Dependence of
1098 phytoplankton carbon isotopic composition on growth rate and [CO₂]_{aq}: Theoretical
1099 considerations and experimental results. *Geochimica et Cosmochimica Acta* **59**, 1131-
1100 1138.
- 1101 Lehmann, M. F., Bernasconi, S.M., Barbieri, A., and McKenzie, J.A. (2002) Preservation of
1102 organic matter and alteration of its carbon and nitrogen isotope composition during
1103 simulated and in situ early sedimentary diagenesis. *Geochimica et Cosmochimica Acta*
1104 **66**, 3573-3584.
- 1105 Leinweber, P., Kruse, J., Walley, F.L., Gillespie, A., Eckhardt, K.-U., Blyth, R.I.R., and Regier, T.
1106 (2007) Nitrogen K-edge XANES – An overview of reference compounds used to
1107 identify ‘unknown’ organic nitrogen in environmental samples. *Journal of*
1108 *Synchrotron Radiation* **14**, 500-511.
- 1109 Lepland, A., Joosu, L., Kirsimäe, K., Prave, Romashkin, A.E., Crne, A.E., Martin, A.P., Fallick,
1110 A.E., Somelar, P., Upraus, K., Mand, K., Roberts, N.M.W., van Zuilen, M.A., Wirth, R.,
1111 Schreiber, A. (2013) Potential influence of sulphur bacteria on Palaeoproterozoic
1112 phosphogenesis. *Nature Geoscience* **7**, 20-24.
- 1113 Lepot, K., Benzerara, K., Brown, G.E., and Philippot, P. (2008) Microbially influenced
1114 formation of 2,724-million-year-old stromatolites. *Nature Geoscience* **1**, 1-4.
- 1115 Lepot, K., Benzerara, K., Rividi, N., Cotte, M., Brown, G.E., and Philippot, P. (2009) Organic
1116 matter heterogeneities in 2.72 Ga stromatolites: Alteration versus preservation by sulfur
1117 incorporation. *Geochimica et Cosmochimica Acta* **73**, 6579-6599.
- 1118 Macko, S. A., Fogel, M. L., Hare, P. E., and Hoering, T. C. (1987) Isotopic fractionation of
1119 nitrogen and carbon in the synthesis of amino acids by microorganisms. *Chem. Geol.* **65**,

- 1120 79-92.
- 1121 Malmberg, P., Bexell, U., Eriksson, C., Nygren, H., and Richter, K., (2007) Analysis of bone
 1122 minerals by time-of-flight secondary ion mass spectrometry. *Rapid Comm. Mass*
 1123 *Spec.* **21**, 745-749.
- 1124 Martin, B., Florke, O.W., and Kainka, E., and Wirth, R. (1996) Electron irradiation damage in
 1125 quartz, SiO₂. *Physics and Chemistry of Minerals* **23**, 409-417.
- 1126 McKenzie, N.R., Hughes, N.C., Myrow, P.M., Banerjee, D.M., Deb, M., and Planavsky, N.J.
 1127 (2013) New age constraints for the Proterozoic Aravalli–Delhi successions of India and
 1128 their implications. *Precambrian Res.*, <http://dx.doi.org/10.1016/j.precamres.2013.10.006>.
- 1129 McKenzie, N.R., Hughes, N.C., Myrow, P.M., Banerjee, D.M., Deb, M., and Planavsky, N.J.
 1130 (2014) Reply to comment on “New age constraints for the Proterozoic Aravalli–Delhi
 1131 successions of India and their implications.” By Melezhik et al. [*Precambrian Res.*],
 1132 *Precambrian Research* **246**, 371-372.
- 1133 Melezhik, V.A., Purohit, R., and Papineau, D. (2014) Comment on “New age constraints for the
 1134 Proterozoic Aravalli–Delhi successions of India and their implications.” By McKenzie et
 1135 al. [*Precambrian Res.* 238 (2013) 120-128], *Precambrian Research* **246**, 319-320.
- 1136 Melezhik, V.A., Fallick, A.E., Medvedev, P.V., Makarikhin, V.V. (1999) Extreme ¹³C_{carb}
 1137 enrichment in ca. 2.0 Ga magnesite-stromatolite-dolomite-‘red beds’ association in a
 1138 global context: a case for the worldwide signal enhanced by a local environment. *Earth*
 1139 *Science Reviews* **48**, 71-120.
- 1140 Melezhik, V.A., Fallick, A.E., Hanski, E.J., Kump, L.R., Lepland, A., Prave, A.R., and Strauss,
 1141 H. (2005) Emergence of the aerobic biosphere during the Archean-Proterozoic transition:
 1142 challenges of future research. *GSA Today* **15**, 4-11.

1
2
3 1143 Minagawa, M. and Wada, E. (1986) Nitrogen isotope ratios of the red tide organisms in the East
4
5 1144 China Sea: A characterization of biological nitrogen fixation. *Marine Chemistry* **19**, 245-
6
7 1145 259.
8
9
10 1146 Mingram, B. and Bräuer, K. (2001) Ammonium concentration and nitrogen isotope composition
11
12 1147 in metasedimentary rocks from different tectonometamorphic units of the European
13
14 1148 Variscan Belt. *Geochim. Cosmochim. Acta* **65**, 273-287.
15
16
17 1149 Mossman, D.J., Gauthier-Lafaye, F., and Jackson, S.E. (2005) Black shales, organic matter, ore
18
19 1150 genesis and hydrocarbon generation in the Paleoproterozoic Franceville Series, Gabon.
20
21 1151 *Precambrian Research* **137**, 253-272.
22
23
24 1152 Nabelek, P.I. (1991) Stable isotope monitors. In: Kerrick, D.M. (ed.) Contact Metamorphism,
25
26 1153 *Reviews in Mineralogy* **26**, Mineralogical Society of America, pp. 395–435.
27
28
29 1154 Nagy, R. M., Porter, S., M., Dehler, C. M., Shen, Y. (2009) Biotic turnover driven by
30
31 1155 eutrophication before the Sturtian low-latitude glaciation. *Nature Geoscience* **2**, 415-418.
32
33
34 1156 Neumann, T., Stogbauer, A., Walpersdorf, E., Stuben, D., Kunzendorf, H. (2002) Stable
35
36 1157 isotope in recent sediments of Lake Arendsee, NE Germany: Reponse to
37
38 1158 eutrophication and remediation measures. *Palaeogeogr., Palaeoclim., Palaeoecol.*
39
40 1159 **178**, 75-90.
41
42
43 1160 Norholt, A.J.G. and Sheldon, R.P. (1986) Proterozoic and Cambrian phosphorites – regional
44
45 1161 review: world resources. In P.J. Cook, Shergold, J.H. (Eds.), Phosphate Deposits of the
46
47 1162 World, volume 1, Proterozoic and Cambrian Phosphorites. Cambridge University Press,
48
49 1163 New York, pp. 9-19.
50
51
52
53 1164 O’Brien, G.W., Harris, J.R., Milnes, A.R., and Veeh, H.H. (1981) Bacterial origin of East
54
55 1165 Australian continental margin phosphorites. *Nature* **294**, 442-444.
56
57
58
59
60

- 1
2
3 1166 O'Brien G.W. and Veeh, H.H. (1980) Holocene phosphorite on the East Australian continental
4
5
6 1167 margin. *Nature* **288**, 690-692.
7
8 1168 Papineau, D., Walker, J.J., Mojzsis, S.J. and Pace, N.R. (2005) Composition and structure of
9
10 1169 microbial communities from stromatolites of Hamelin Pool in Shark Bay, Western
11
12 1170 Australia. *Applied and Environmental Microbiology* **71**, 4822-4832.
13
14
15 1171 Papineau, D., Purohit, R., Goldberg, T., Pi, D., Shields, G.A., Bhu, H., Steele, A., and Fogel,
16
17 1172 M.L. (2009) High primary productivity and nitrogen cycling after the Paleoproterozoic
18
19 1173 phosphogenic event in the Aravalli Supergroup, India, *Precambrian Research* **171**, 37-
20
21 1174 56.
22
23
24 1175 Papineau, D. (2010) Global biogeochemical changes at both ends of the Proterozoic: Insights
25
26 1176 from phosphorites, *Astrobiology* **10**, 1-17.
27
28
29 1177 Papineau, D., DeGregorio, B.T., Cody, G.D., Fries, M.D., Mojzsis, S.J., Steele, A., Stroud, R.M.,
30
31 1178 and Fogel, M.L. (2010a) Ancient graphite in the Eoarchean quartz-pyroxene rock from
32
33 1179 Akilia in southwest Greenland I: Petrographic and spectroscopic characterization.
34
35 1180 *Geochimica et Cosmochimica Acta* **74**, 5862-5883.
36
37
38 1181 Papineau, D., DeGregorio, B.T., Stroud, R.M., Steele, A., Pecoits, E., Konhauser, K., Wang, J.,
39
40 1182 and Fogel, M.L. (2010b) Ancient graphite in the Eoarchean quartz-pyroxene rock from
41
42 1183 Akilia in southern West Greenland II: Isotopic and chemical compositions and
43
44 1184 comparison with Paleoproterozoic banded iron formations. *Geochimica et Cosmochimica*
45
46 1185 *Acta* **74**, 5884-5905.
47
48
49
50 1186 Papineau, D., Purohit, R., Fogel, M.L., and Shields, G.A. (2013) High phosphate availability as a
51
52 1187 possible cause for massive cyanobacterial production of oxygen in the Proterozoic
53
54 1188 atmosphere. *Earth and Planetary Science Letters* **362**, 225-236.
55
56
57
58
59
60

1
2
3 1189 Peters, K.E., Sweeney, R.E., and Kaplan, I.R. (1978) Correlation of carbon and nitrogen stable
4
5 1190 isotope ratios in sedimentary organic matter. *Limnol. Oceanogr.* **23**, 598–604.
6
7
8 1191 Piper, D.Z. and Cadispori, L.A. (1975) Marine phosphorite deposits and the nitrogen cycle.
9
10 1192 *Science* **188**, 15-18.
11
12
13 1193 Pufahl, P. and Hiatt, E.. (2012) Oxygenation of the Earth’s atmosphere-ocean system: A review
14
15 1194 of physical and chemical sedimentologic responses. *Marine and Petroloelum Geology* **32**,
16
17 1195 1-20.
18
19
20 1196 Purohit, R., Sanyal, P., Roy, A.B., and Bhattacharya, S.K. (2010) 13C enrichment in the
21
22 1197 Palaeoproterozoic carbonate rocks of the Aravalli Supergroup, northwest India: Influence
23
24 1198 of depositional environment, *Gondwana Research* **18**, 538-546.
25
26
27 1199 Purohit, R., Bhu. H., Mehta, P., and Avadich, P.C. (2012) Tectonistratigraphic status of the
28
29 1200 Proterozoic Babarmal pink marble from the Aravalli Supergroup. *Journal of the*
30
31 1201 *Geological Society of India* **79**, 1-16.
32
33
34 1202 Rao, V.P., Naqvi, S.W.A., Kumar, M.D., Cardinal, D., Michard, A., Borole, D.V., Jacobs, E.,
35
36 1203 and Natarajan, R. (2000) A comparative study of Pleistocene phosphorites from the
37
38 1204 continental slope off western India. *Sedimentology* **47**, 945-960.
39
40
41 1205 Roy, A.B. and Jakhar, S.R. (2002) Geology of Rajasthan (Northwest India) Precambrian to
42
43 1206 recent. Scientific Publishers (India), 421p.
44
45
46 1207 Roy, A.B. and Paliwal, B.S. (1981) Evolution of lower Proterozoic epicontinental deposits:
47
48 1208 stromatolites-bearing Aravalli rocks of Udaipur, Rajasthan, India. *Precamb. Res.* **14**, 49-
49
50 1209 74.
51
52
53 1210 Roy, A.B., Purohit, R., (2015) Lithostratigraphic, Geochronologic, and Depositional framework
54
55 1211 of the Precambrian basins of the Aravalli Mountains and adjoining areas, Rajasthan,
56
57
58
59
60

- 1212 India., In: Mazumder, R. & Eriksson, P. G. (eds) Precambrian Basins of India:
1213 Stratigraphic and Tectonic Context. Geological Society, London, Memoirs: Chapter 4,
1214 43, 55–66.
- 1215 Sanchez-Navas, A. and Martin-Algarra, A. (2001) Genesis of apatite in phosphate stromatolites.
1216 *European Journal of Mineralogy* **13**, 361-376.
- 1217 Sanchez-Navas, A., Martin-Algarra, A., and Nieto, F. (1998) Bacterially-mediated authigenesis
1218 of clays in phosphate stromatolites. *Sedimentology* **45**, 519-533.
- 1219 Sarangi, S., Gopalan, K., Roy, A.B., Sreenivas, B., and Das Sharma, S. (2006) Pb-Pb age of the
1220 carbonates of Jhamarkotra Formation constraining the age of the Aravalli Supergroup,
1221 Rajasthan. *J. Geol. Soc. India* **67**, 442-446.
- 1222 Schopf, J.W. and Kudryatsev, A.A. (2010) A renaissance in studies of ancient life. *Geology*
1223 Today **26**, 140-145.
- 1224 Semikatonov, M.A., Raaben, M.E., Sergeev, V.N., Veis, A.F., and Artemova, O.V. (1999) Biotic
1225 events and positive dC_{carb} anomaly at 2.3-2.06 Ga. *Stratigraphy and Geological*
1226 *Correlation* **7**, 413-436.
- 1227 Shard, A.G., Whittle, J.D., Beck, A.J., Brookes, P.N., Bullett, N.A., Talib, R.A., Mistry, A.,
1228 Barton, D., and McArthur, S.L. (2004) A NEXAFS examination of unsaturation in
1229 plasma polymers of allylamine and propylamine. *Journal of Physical Chemistry B* **108**,
1230 12472-12480.
- 1231 She, Z., Strother, P., and Papineau, D. (2014) Terminal Proterozoic cyanobacterial blooms and
1232 phosphogenesis documented by the Doushantuo granular phosphorites II: petrology and
1233 carbon isotopes. *Precambrian Research* **251**, 62-79.

1
2
3 1234 She, Z., Strother, P., McMahon, G., Nittler, L.R., Wang, J., Zhang, J., Longkang, S., Ma, C., and
4
5 1235 Papineau, D. (2013) Terminal Proterozoic cyanobacterial blooms and phosphogenesis
6
7 1236 documented by the Doushantuo granular phosphorites I: *In situ* micro-analyses of
8
9 1237 textures and composition. *Precambrian Research* **235**, 20-35.
10
11 1238 Shields, G.A., Strauss, H., Howe, S.S., Siegmund, H. (1999) Sulphur isotope compositions of
12
13 1239 sedimentary phosphorites from the basal Cambrian of China: implications for
14
15 1240 Neoproterozoic-Cambrian biogeochemical cycling. *Journal of the Geological Society of*
16
17 1241 *London* **156**, 943-955.
18
19 1242 Schulz, K.J., and Cannon, W.F., 2007, The Penokean orogeny in the Lake Superior region:
20
21 1243 *Precambrian Research* **157** , 4–25.
22
23 1244 Sreenivas, B., Das Sharma, S., Kumar, B., Patil, D.J., Roy, A.B. and Srinivasan, R. (2001)
24
25 1245 Positive d¹³C excursion in carbonate and organic fractions from the Paleoproterozoic
26
27 1246 Aravalli Supergroup, Northwestern India. *Precamb. Res.* **106**, 277-290.
28
29 1247 Strother, P. Battison, L., Brasier, M., and Wellman, C.H. (2011) Earth’s earliest non-marine
30
31 1248 eukaryotes. *Nature* **472**, 505-509.
32
33 1249 Sun, S., Chan, L.S., and Li, Y.-L. (2014) Flower-like apatite recording microbial processes
34
35 1250 through deep geological time and its implication to the search for mineral records of
36
37 1251 life on Mars. *American Mineralogist* **90**, 2116-2125.
38
39 1252 Thiel, V. and Sjövall, P. (2011) Time-of-Flight Secondary Ion Mass Spectrometry (TOF-
40
41 1253 SIMS) Principles and Practice in the Biogeosciences. In: Grice, K. and Keely, B. (eds.),
42
43 1254 Principles and Practice of Analytical Techniques in Geosciences. 1-36.
44
45 1255 Thomazo, C. and Papineau, D. (2013) The evolution of the nitrogen cycle on the early Earth.
46
47 1256 *Elements* **9**, 345-351.
48
49
50
51
52
53
54
55
56
57
58
59
60

- 1
2
3 1257 Urquhart, S.G., and Ade, H. (2002) Trends in the carbonyl core (C 1S, O 1S) $\rightarrow \pi^*_{C=O}$
4
5
6 1258 transition in the near-edge X-ray absorption fine structure spectra of organic
7
8 1259 molecules. *Journal of Physical Chemistry B* **106**, 8531-8538.
9
10
11 1260 Vairavamurthy, A., and Wang, S. (2002) Organic nitrogen in geomacromolecules: Insights
12
13 1261 on speciation and transformation with K-edge XANES spectroscopy. *Environmental*
14
15 1262 *Science and Technology* **36**, 3050-3056.
16
17
18 1263 Vasconcelos, C., Warthmann, R. McKenzie, J.A., Visscher, P.T., Bittermann, A.G., and van Lith,
19
20 1264 Y. (2006) Lithifying microbial mats in Lagoa Vermelha, Brazil: Modern Precambrian
21
22 1265 relics? *Sedimentary Geology* **185**, 175-183.
23
24
25 1266 Wacey, D., Menon, S., Green, L., Gerstmann, D., Kong, C., McLoughlin, N., Saunders, M., and
26
27 1267 Brasier, M. (2012) Taphonomy of very ancient microfossils from the 3400Ma Strelley
28
29 1268 Pool Formation and 1900 Ma Gunflint Formation: New insights using a focused ion
30
31 1269 beam. *Precambrian Research* **220-221**, 234-250.
32
33
34 1270 Williford, K.H., Ushikubo, T., Schopf, J.W., Lepot, K., Kitajima, K., and Valley, J.W. (2013)
35
36 1271 Preservation and detection of microstructural and taxonomic correlations in the carbon
37
38 1272 isotopic compositions of individual Precambrian microfossils. *Geochimica et*
39
40 1273 *Cosmochimica Acta* **104**, 165-182.
41
42
43 1274 Wirth, R. (2009) Focused Ion Beam (FIB) combined with SEM and TEM: Advanced analytical
44
45 1275 tools for studies of chemical composition, microstructure and crystal structure in
46
47 1276 geomaterials on a nanometer scale. *Chemical Geology* **261**, 217-229.
48
49
50
51 1277 Xiao, S., Zhang, Y., and Knoll, A. H. (1998) Three-dimensional preservation of algae and animal
52
53 1278 embryos in a Neoproterozoic phosphorite. *Nature* **391**, 553-558.
54
55
56
57
58
59
60

1
2
3 1279 Xiao, S., Hagadorn, J. W., Zhou, C., and Yuan, X. (2007) Rare helical spheroidal fossils from the
4
5 1280 Doushantuo Lagerstätte: Ediacaran animal embryos come of age? *Geology* **35**, 115-118.
6
7
8 1281 Xue, Y.S., Tang, T.F., and Yu, C.L. (1999) “Animal embryos”, a misinterpretation of
9
10 1282 Neoproterozoic microfossils. *Acta Micropalaeontologica Sinica* **16**, 1–4.
11
12
13 1283 Yin, L., Zhu, M., Knoll, A.H., Yuan, X., Zhang, J., and Hu, J. (2007) Doushantuo embryos
14
15 1284 preserved inside diapause egg cysts. *Nature* **446**, 661-663.
16
17
18 1285 Zega, T.J., Nittler, L.R., Busemann, H., Hoppe, P., and Stroud, R.M. (2007) Coordinated isotopic
19
20 1286 and mineralogic analyses of planetary materials enabled by in situ lift-out with a focused
21
22 1287 ion beam scanning electron microscope. *Met. Planet. Sci.* **42**, 1-14.
23
24
25 1288 Zerkle, A.L., Junium, C.K., and Canfield, D.E. (2008) Production of 15N-depleted biomass
26
27 1289 during cyanobacterial N2-fixation at high Fe concentrations. *Journal of Geophysical*
28
29 1290 *Research* **113**, doi:10.1029/2007JG000651.
30
31
32 1291 Zhang, X., Sigmna, D.M., Morel, F.M.M., and Kraepiel, A.M.L. (2014) Nitrogen isotope
33
34 1292 fractionation by alternative nitrogenases and past ocean anoxia. *P.N.A.S.* **11**, 4782-4787.
35
36 1293
37
38 1294
39
40 1295
41
42 1296
43
44 1297
45
46 1298
47
48 1299
49
50 1300
51
52 1301
53
54
55
56
57
58
59
60

1
2
3
4
5
6
7
8
9
10
11
12
13
14
15
16
17
18
19
20
21
22
23
24
25
26
27
28
29
30
31
32
33
34
35
36
37
38
39
40
41
42
43
44
45
46
47
48
49
50
51
52
53
54
55
56
57
58
59
60

1302	Table 1: Samples analysed by various analytical techniques in this study.
1303	
1304	Table 2: Raman spectral data of representative rosettes and microbial mats in the Aravalli
1305	phosphorites.
1306	
1307	Table 3: Stable isotope compositions of decarbonated micro-drilled powders from the Badagaon
1308	stromatolitic phosphorites.
1309	
1310	Table 4: Peaks detected by STXM at the C, N, and O edges.
1311	
1312	Table 5: Peaks and masses detected by ToF-SIMS on the FIB lamella from sample UV0602.
1313	

Figure 1

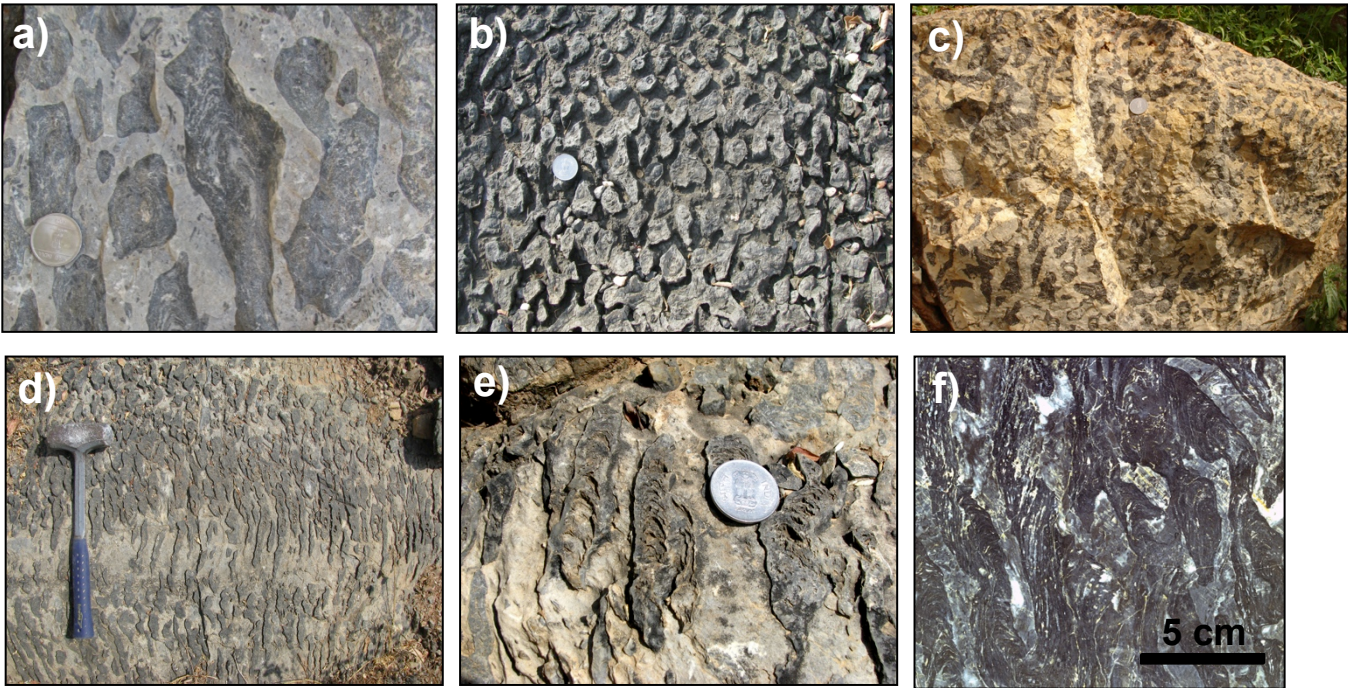


Figure 1: Images of columnar and columnar branching stromatolitic phosphorites from the Badagaon locality (a-c), the Jhamarkotra mine (d-e), and from a polished slab (f). Phosphatic columns on weathered surfaces have high topographic relief. Coin is 28 mm in diameter.

Figure 2

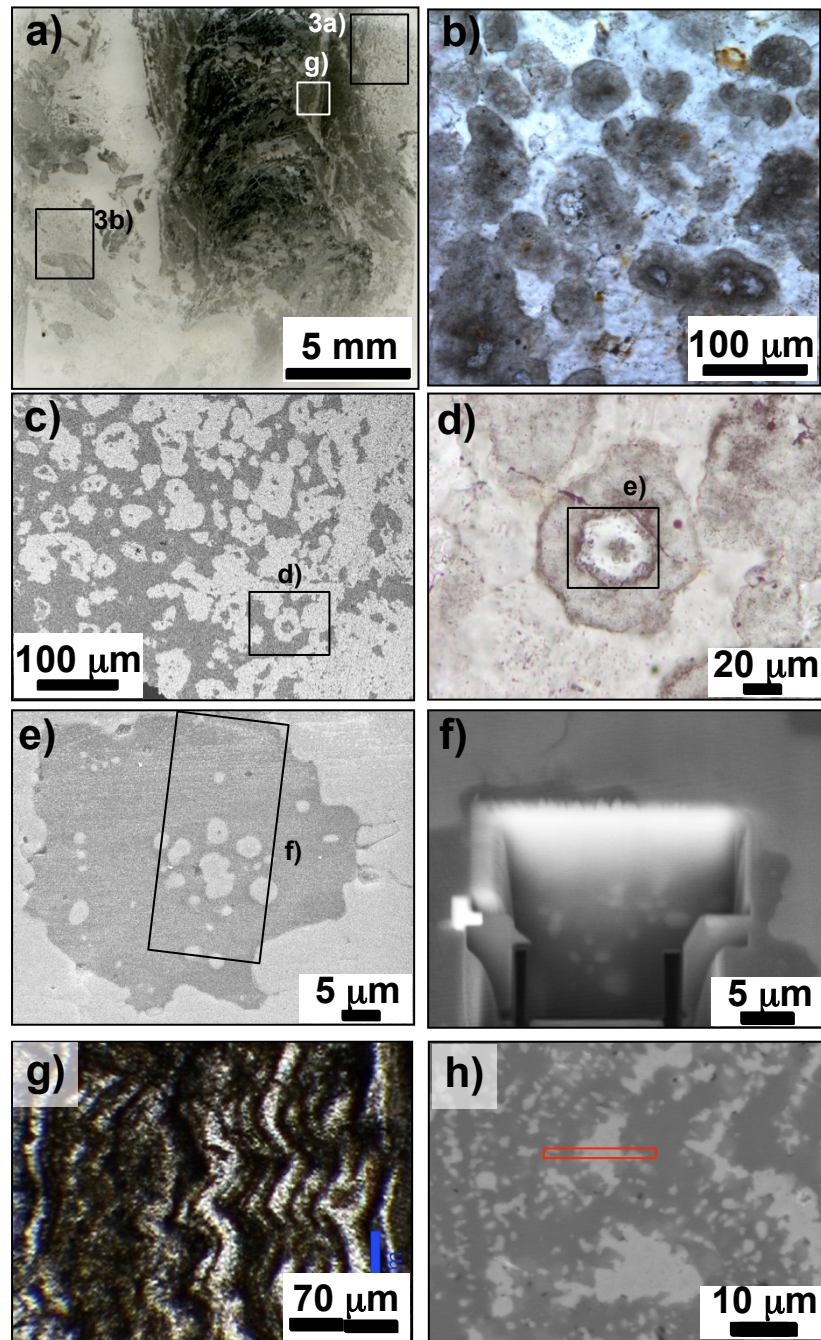


Figure 2: Photomicrographs in transmitted light (a, b, d, g), backscattered electrons (c), and secondary electrons (e, f, h) of a stromatolitic phosphorite from Badagaon. The intercolumnar space contains fields of apatite rosettes embedded in dolomite (b, c). Most (all?) apatite rosettes contain a core of chert with micron-size spheroidal inclusions of apatite (e, f). g) microbial mat in stromatolite column with organic-apatite layers interspaced with dolomite-calcite layers. h) Microbial mat in g), and the site of nano-fabrication, with apatite layers in light grey and interlayers carbonate in darker grey.

Figure 3

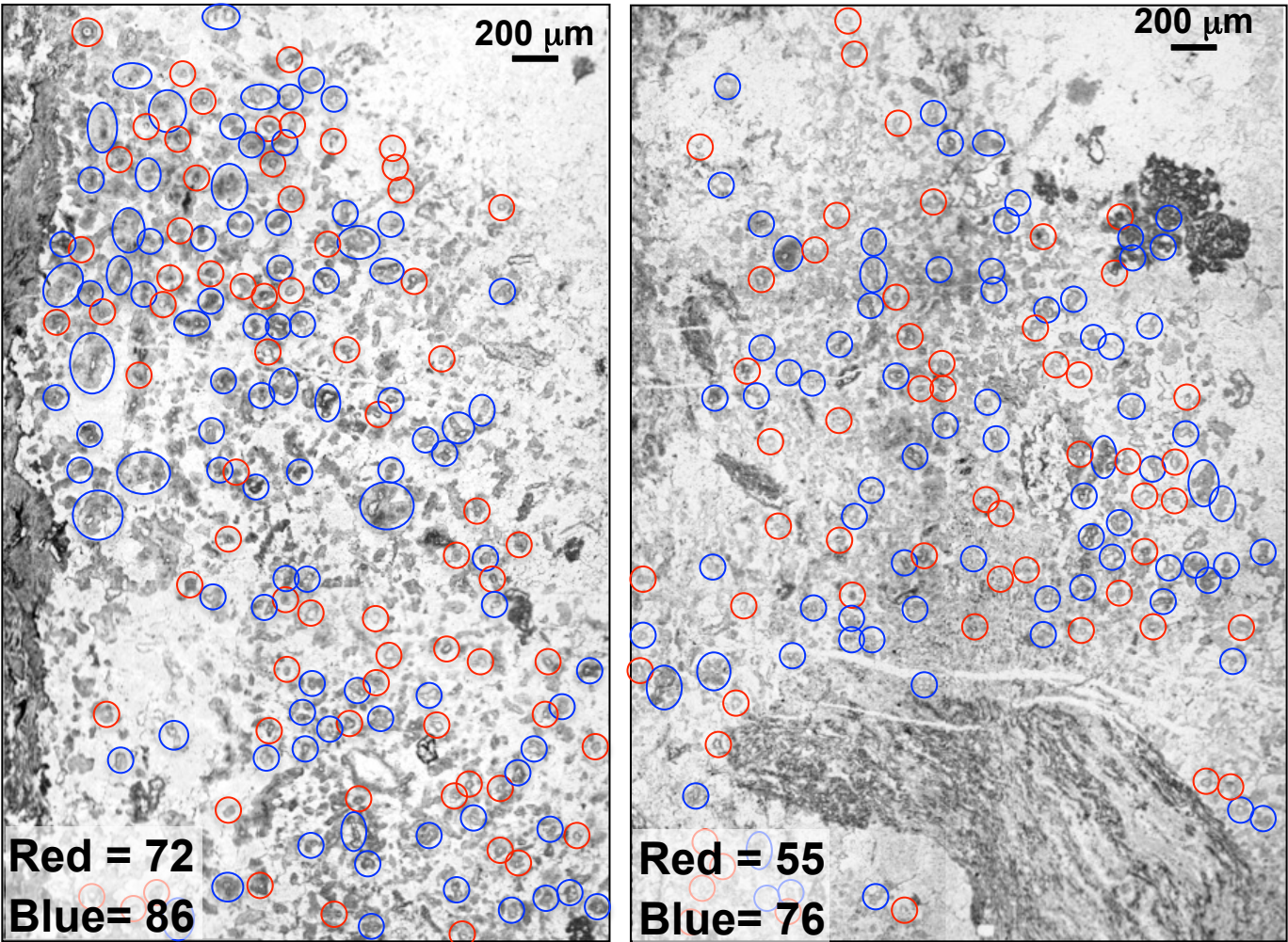


Figure 3: Transmitted light images of two maps at 100X of stromatolite (Badagaon) intercolumnar spaces of dolomitic areas that highlights rounded microstructures (rosettes) made of carbonate fluorapatite and organic matter (grayish-darker phase) surrounding individual cores of chert (see Raman maps in Figure 4). Red circle are individual rounded microstructures and blue circle are groups of 2 to 5 rounded structures. Figures a) and b) relate to the locations shown in the thin section in Figure 2.

Figure 4

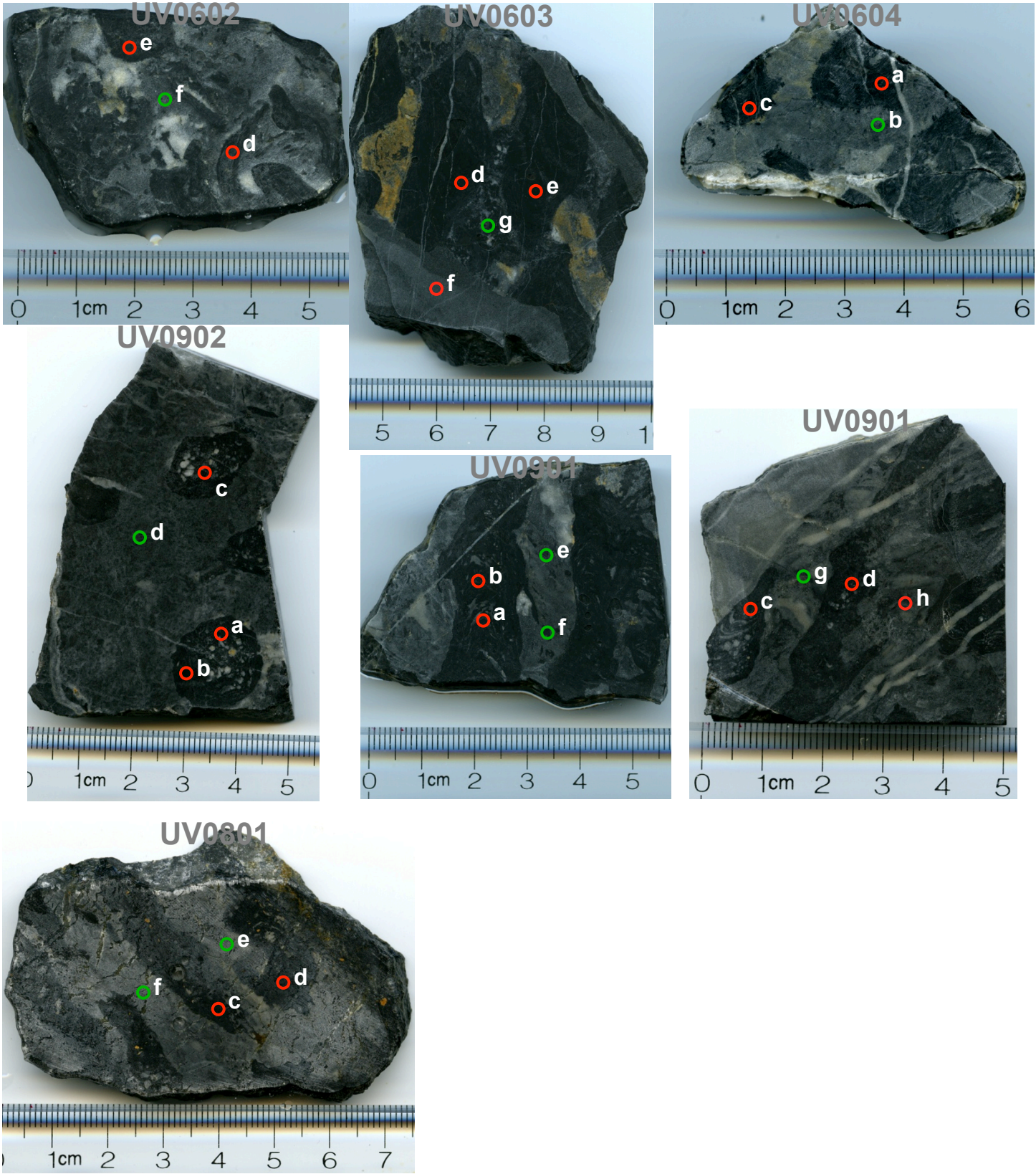


Figure 4: Photographs of selected slabs of stromatolitic phosphorites from Badagaon showing the locations of micro-drilled spots and the corresponding analysis spots (2.1 mm in diameter; green is intercolumn and red is column). Full isotope data is shown in Table 2.

Figure 5

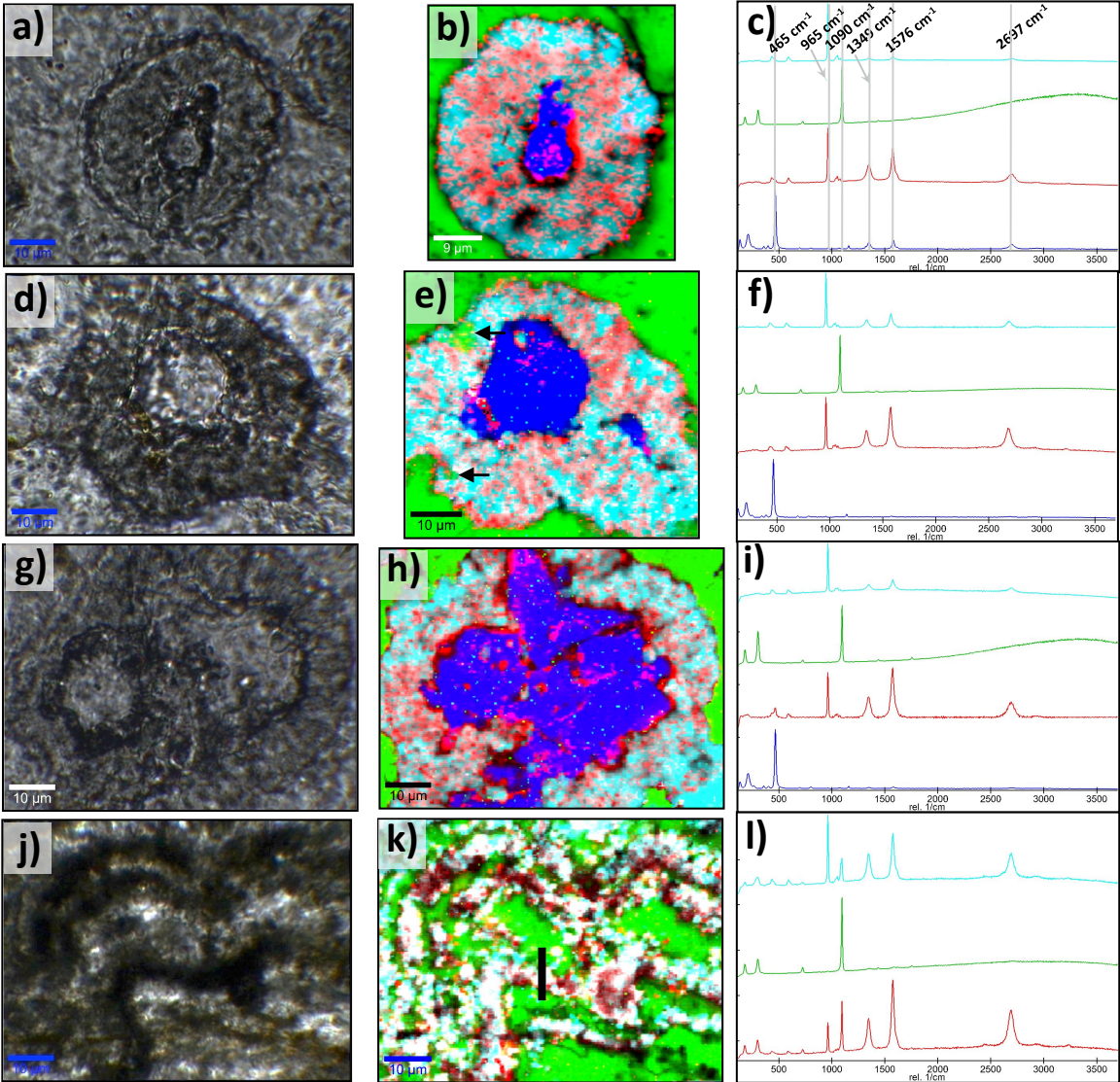


Figure 5: Representative examples of transmitted light photomicrographs (a, d, g, j), Raman images (b, e, h, k) and spectra (c, f, i, l) of three occurrences of apatite rosettes with chert cores in the intercolumnar and a finely laminated microbial mat from a stromatolite column. Colors used for Raman images and spectra are red for the intensity of G-band (carbonaceous material – white when signal is saturated with turquoise as in k), turquoise for the 965 cm⁻¹ peak of apatite, blue for the 467 cm⁻¹ peak of quartz, and green for the 1097 cm⁻¹ peak of dolomite. White pixels in Raman images have high total counts with both carbonaceous material and apatite. The black line in k) shows the location of the lift-out foil (Fig. 7).

Figure 6

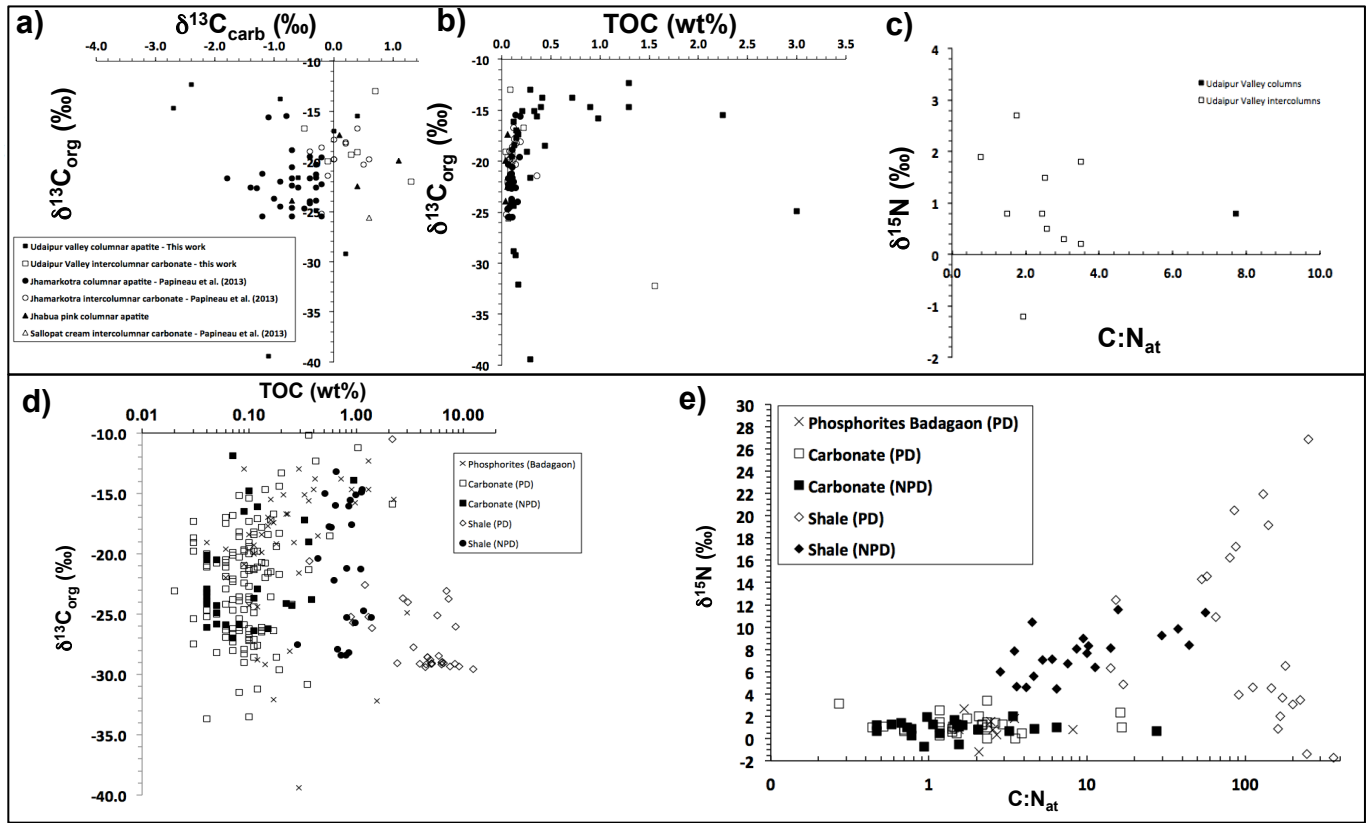


Figure 6: Comparison plots of isotopic compositions of organic matter, carbonate, and nitrogen with total organic carbon and nitrogen, and the atomic C/N ratio. a-b) Plots for organic matter, carbonate in stromatolitic phosphorites from Jhamarkotra, Badagaon, Jhabua, and Sallopat, c) Nitrogen compositions of acidified stromatolitic phosphorites from Badagaon, d) Composition of organic matter in the carbonates and shales of the Phosphate Domain and Non-Phosphate Domain; e) plots of $\delta^{15}\text{N}_{\text{TN}}$ versus C/N_{atomic} for the Badagaon phosphorites with comparisons from shales and carbonates. Source of data for carbonates and shales come from Papineau et al., 2013; 2009, respectively.

Figure 7

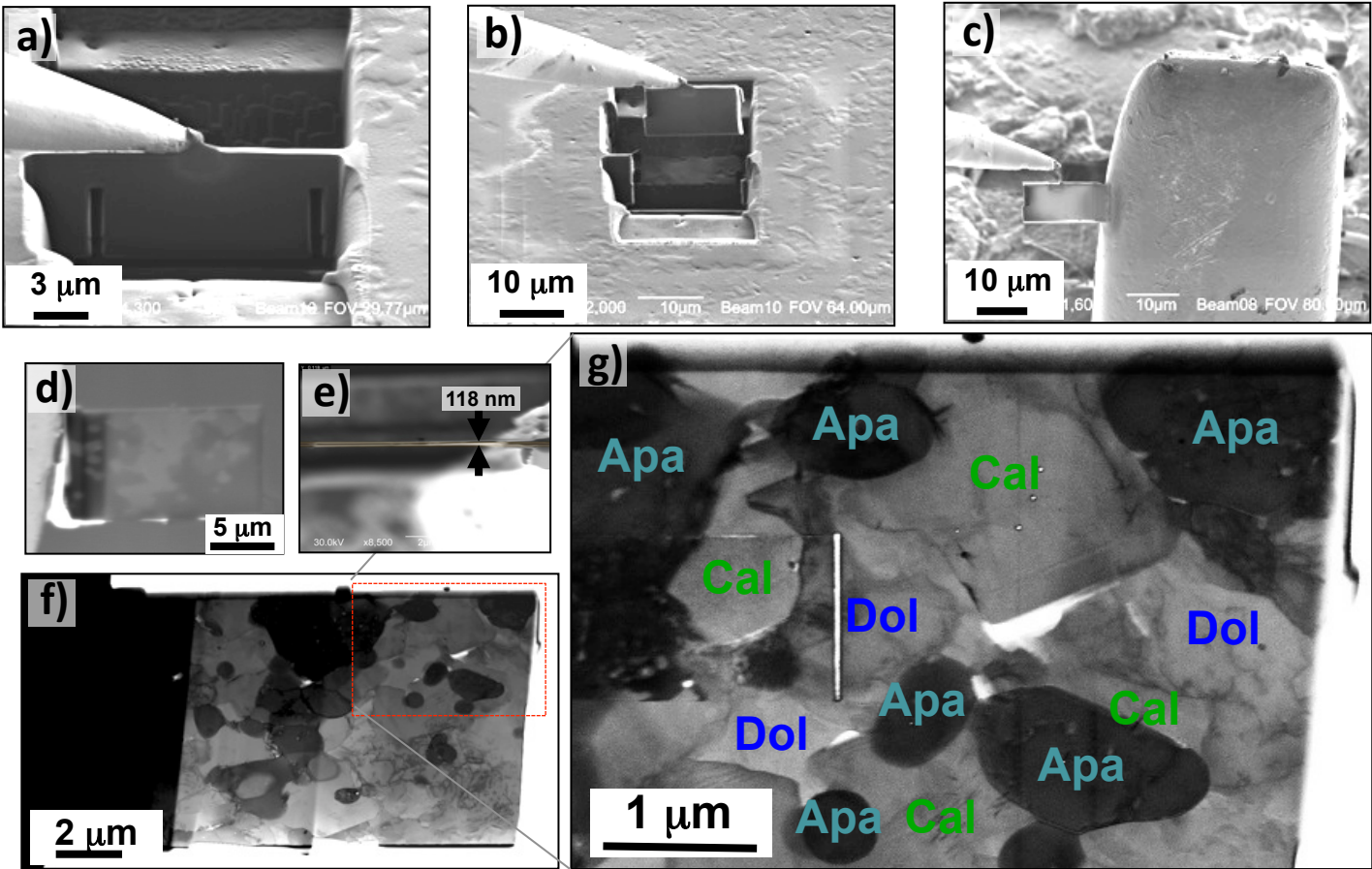


Figure 7: a-e) secondary electron images of the micro-fabricated FIB foil, f-g) bright field TEM images of the nanoscale phases in the microbial mat (Apa = apatite, Cal = calcite, and Dol = dolomite).

Figure 8

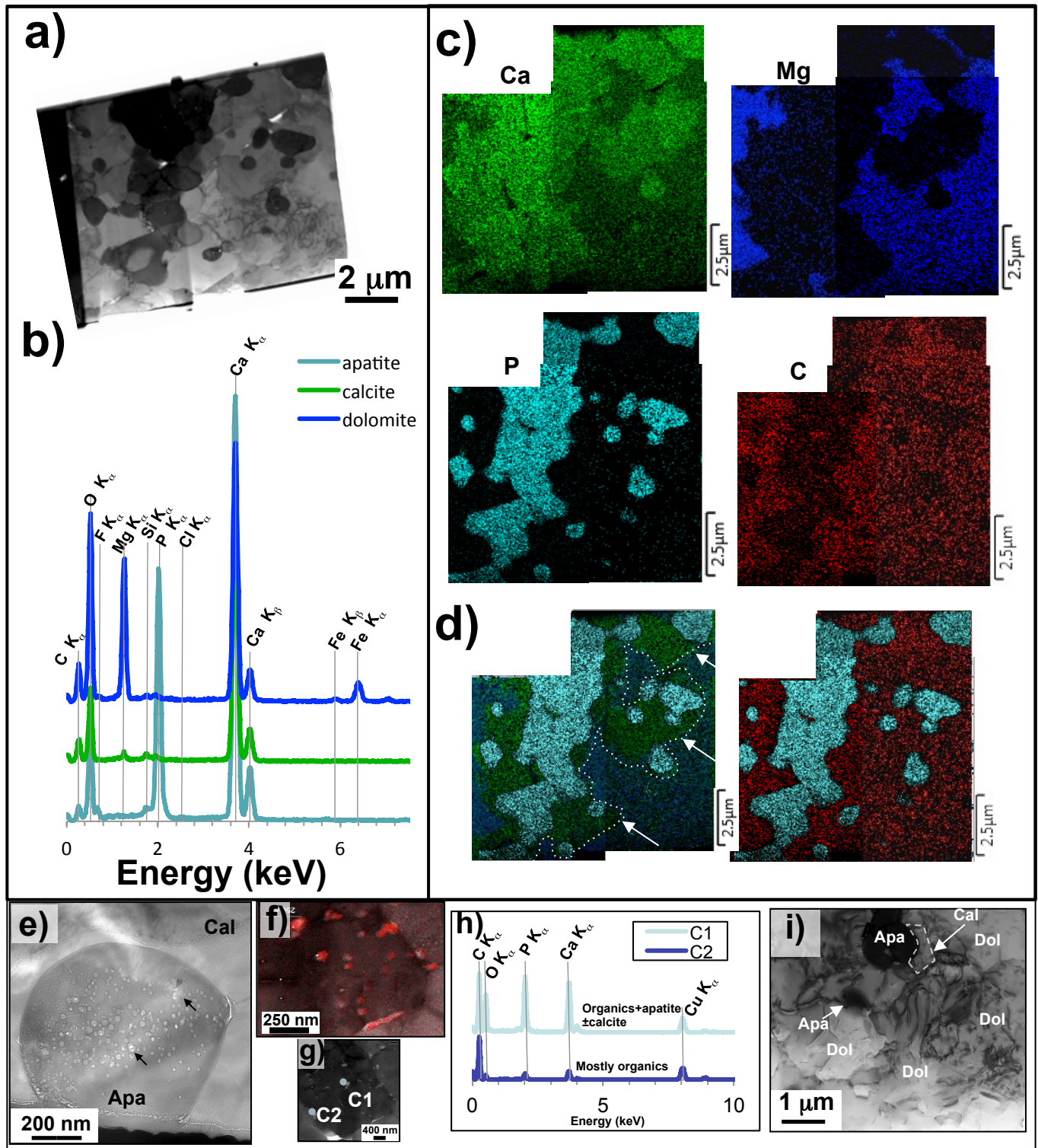


Figure 8: Scanning transmission electron microscopy data from FIB foil seen a) in bright field; b) Energy dispersive spectra, c) K_{α} line intensity images of Ca, Mg, P, and C; d) overlain K_{α} line intensity images for Ca, Mg, and P and for C and P with two white arrows highlighting the tangential extensions, e) example of microscopic spheroidal grain of apatite with electron beam damage (two examples are shown with white arrows), presumably from the decomposition of water in apatite, and f) with organic inclusions (with red overlay of a C-EDS map). g) apatite layer with two EDS spot analyses shown in h), and i) lower right corner area of the foil in (a) with nanoscale veins or cracks in dolomite.

Figure 9

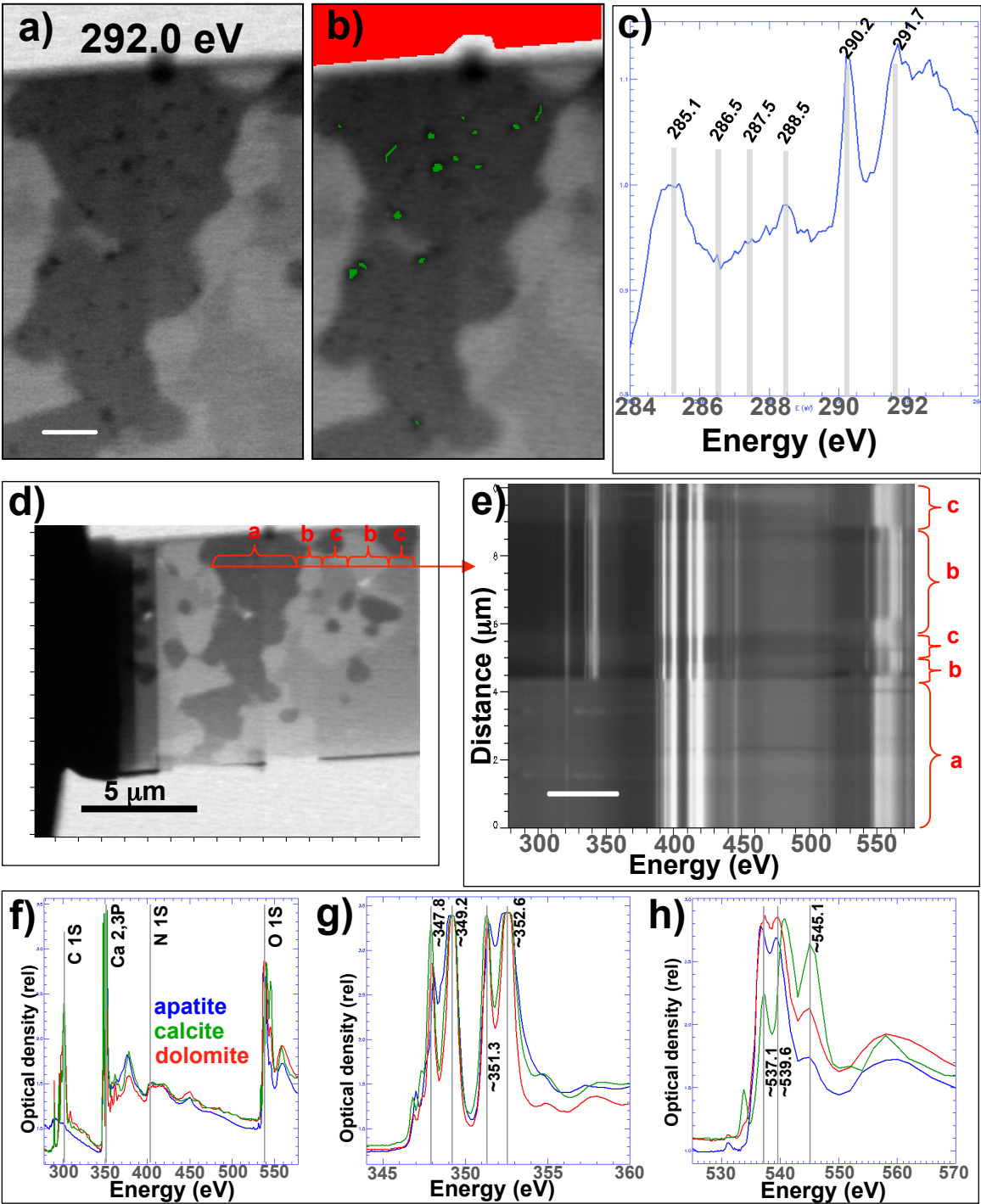


Figure 9: Synchrotron-based STXM images and spectra from the FIB foil of a Badagaon stromatolitic phosphorite. a-b) Images of the foil at 292.0 eV with the highlighted green pixels used for the XANES spectrum at the C K-edge in c) (red is for background correction), d) STXM image at 280.0 eV showing the line scanned, e) hyperspectral line scan between 280.0 and 580.0 eV, f) average XANES spectra for the three C-, O-, and Ca-bearing phases for the full bandwidth, g) XANES spectrum for the Ca L-edge, and h) XANES spectra for the O K-edge

Figure 10

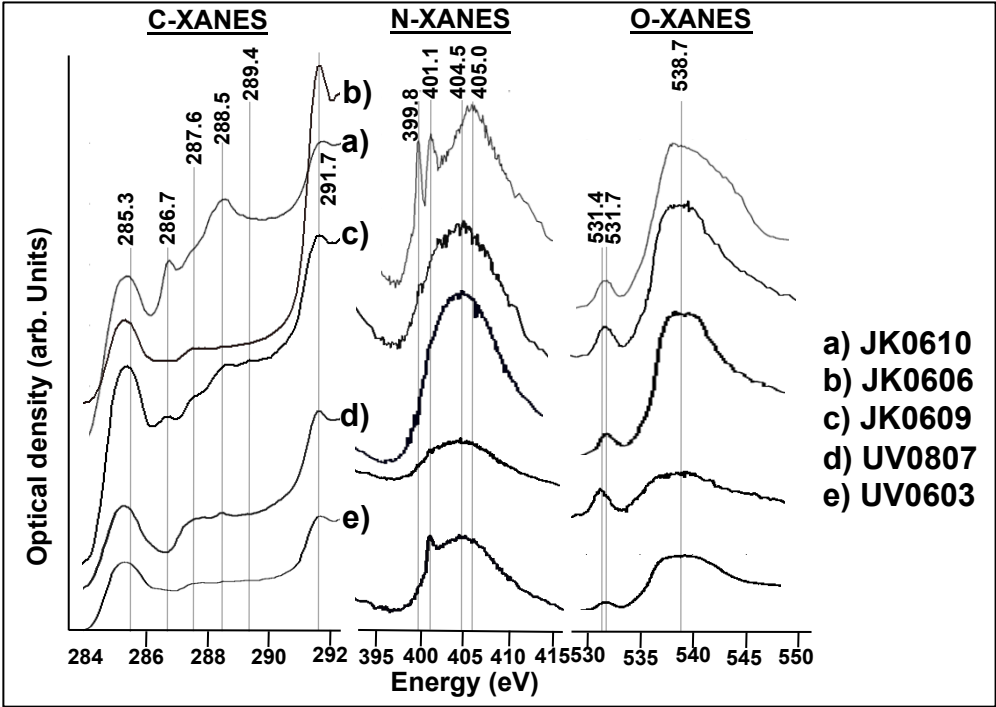


Figure 10: Synchrotron-based STXM spectra of C-, N, and O-XANES for four acid-insoluble residues of organic matter from Aravalli stromatolitic phosphorites (mixed column and intercolumn) from Jhamarkotra (a, b, and c) and Badagaon (d and e).

Figure 11

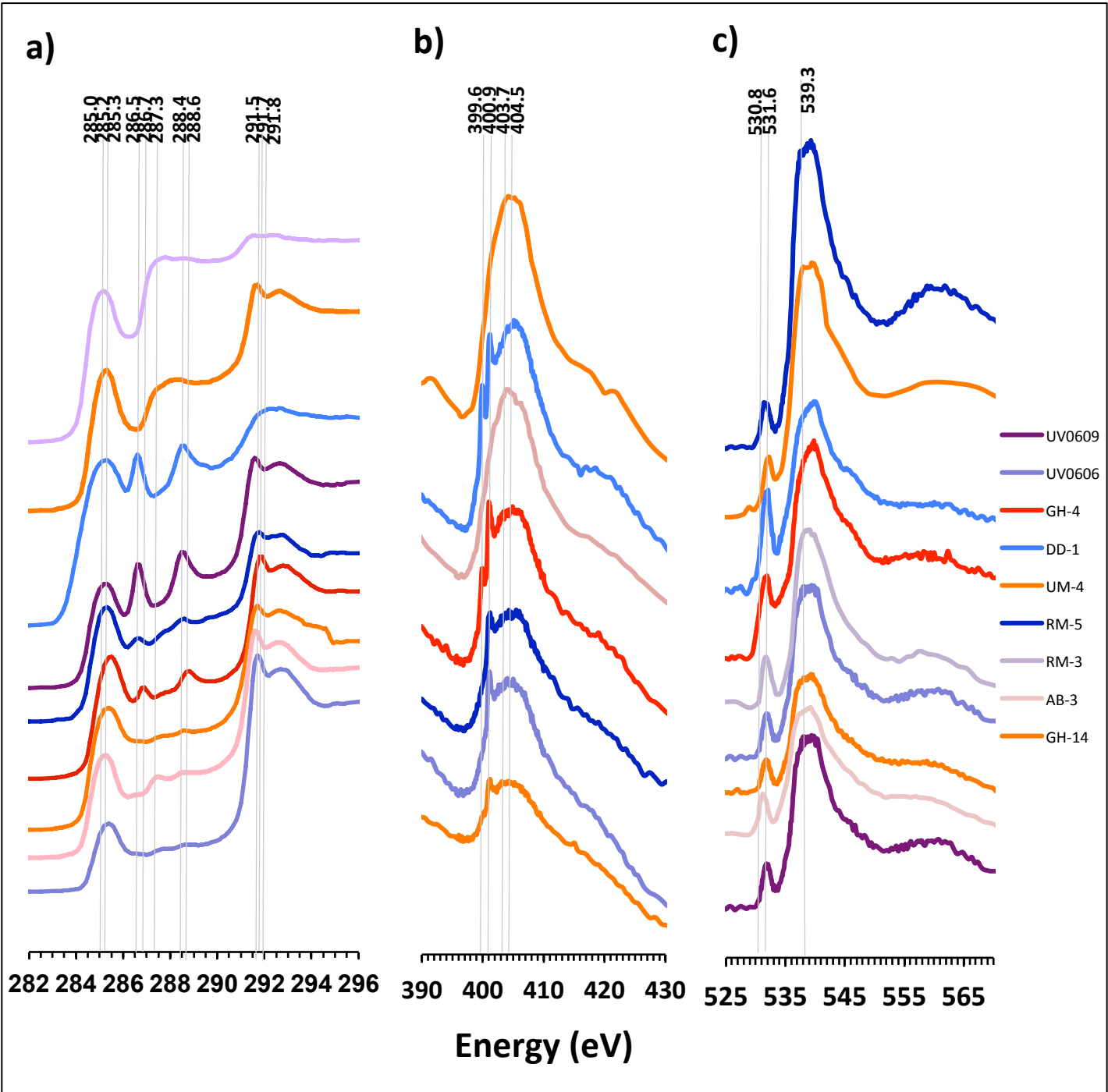


Figure 11: XANES spectra of organic matter in Paleoproterozoic black shales from Aravalli, India with blue-violet colors for the 'Phosphate Domain' and red-orange colours for the 'Non-Phosphate Domain' (blue-purple colours). a) Spectra at the C 1S edge, b) Spectra at the N 1S edge, and c) Spectra at the O 1S edge.

Figure 12

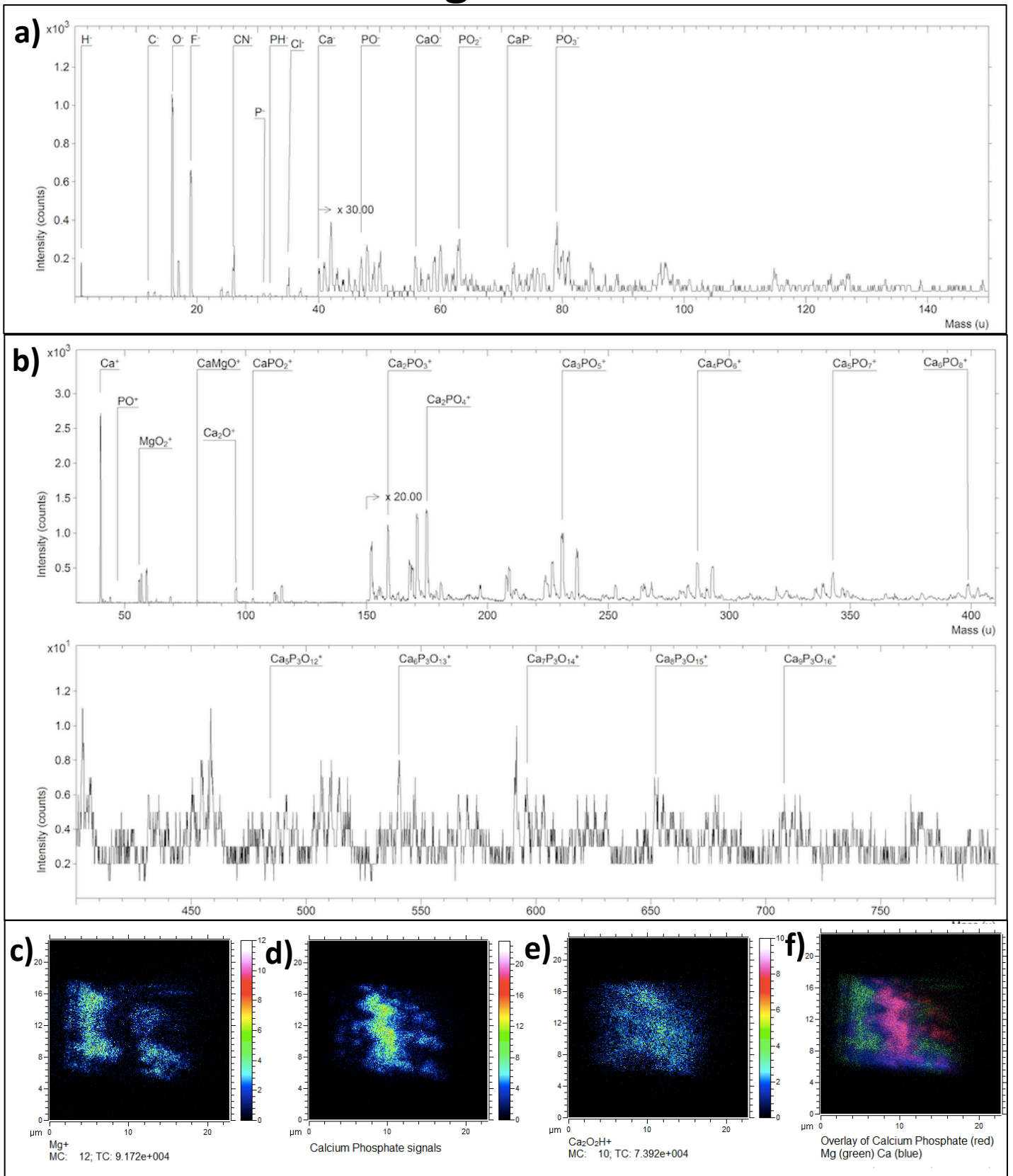


Figure 12: Secondary ion map by ToF-SIMS of molecular fragments from the nano-fabricated microbial mat from the Badagaon stromatolitic phosphorite. a) negative secondary ion spectrum integrated over the entire surface of the foil and b) positive secondary ion spectrum of the same target. c-f) secondary ion images of c) Mg^+ , d) $CaPO^+$, e) $Ca_2O_2H^+$, and f) overlay of $CaPO^+$ (red), Mg^+ (green), Ca^+ (blue).

Figure 13

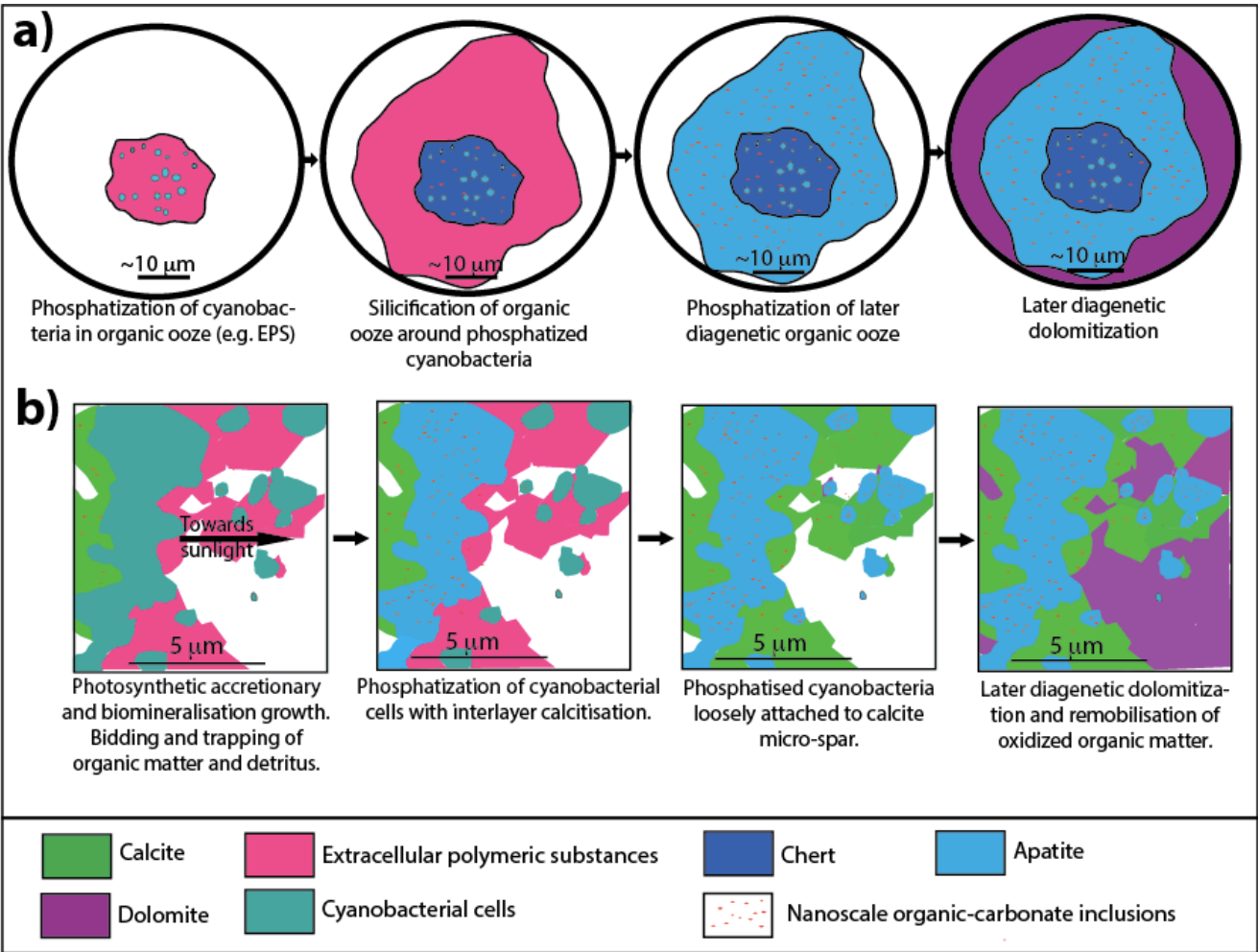


Figure 13: Interpretive schematic representation of the proposed sequence of mineral precipitation for a) intercolumnar rosettes and b) microbial mats in columnar apatite in the Aravalli stromatolitic phosphorites. Hypothetical organic matter composed of EPS and cyanobacteria becomes supersaturated with respect to apatite, which triggers phosphatisation of cyanobacterial cells, silicification (dominantly in intercolumns) and growth over a calcite layer.

Table 1: Samples analysed by various analytical techniques in this study

Sample name	Sample location	Bulk major and minor elements	C and N isotopes of decarbonated powders	C and O isotope of carbonate	Raman	STXM	ToF-SIMS	FIB-STEM
<u>Stromatolitic phosphorite</u>								
UV0602	N: 24o38'22.3" E:73o40'80.0"	X	X	X	X	X	X	X
UV0603	N: 24o38'22.3" E:73o40'80.0"	X	X	X		X		
UV0604	N: 24o38'22.3" E:73o40'80.0"	X	X	X				
UV0605	N: 24o38'22.3" E:73o40'80.0"		X	X				
UV0801	N: 24o38'16.0" E:73o40'36.7"		X	X				
UV0805	Road side of Neematch Mata temple		X	X				
UV0806	N: 24o38'11.4" E:73o40'38.7"		X	X				
UV0807	N: 24o38'11.4" E:73o40'38.7"		X	X		X		
UV0808	N: 24o38'11.4" E:73o40'38.7"	X	X	X				
UV0901	N: 24o37'22.2" E:73o40'44.3"		X					
UV0902	N: 24o37'17.9" E:73o40'44.8"		X					
JK0606	Jhamarkotra mine 'Block B'	X [§]		X [§]		X		
JK0609	Jhamarkotra mine 'Block B'	X [§]		X [§]		X		
JK0610	Jhamarkotra mine 'Block B'	X [§]		X [§]		X		
<u>Carbonaceous shales</u>								
GH-14	Ghasiar	X*	X*		X*	X		
AB-3	Amberi	X*	X*		X*	X		
RM-3	Rama	X*	X*		X*	X		
RM-5	Rama	X*	X*		X*	X		
DD-1	Dhamdhar	X*	X*		X*	X		
GH-4	Ghasiar	X*	X*		X*	X		
UV0606	Amberi	X*	X*		X*	X		
UV0609	Amberi	X*	X*		X*	X		

X* Data published in Papineau et al. (2009)

X[§] Data published in Papineau et al. (2013)

Table 2: Raman spectral data of representative rosettes and microbial mats in the Aravalli phosphorites.

Target	SiO-band position	SiO-band FWHM	PO-band position	PO-band FWHM	CO-band position	CO-band FWHM	D-band position	D-band FWHM	G-band position	G-band FWHM	2D-band position	2D-band FWHM	D-band area*	G-band area*
Rosette 01	467.3	5.8	964.2	4.3	1096.8	4.6	1348.1	17.9	1575.3	10.5	2694.7	7.9	5762.6	9060.9
Rosette 02	467.5	5.8	964.0	8.0	1096.3	4.9	1345.6	12.1	1573.9	10.5	2684.6	20.2	887.0	1401.8
Rosette 03	467.4	5.8	964.0	4.4	1096.7	4.6	1346.6	12.0	1573.9	10.3	2692.9	5.8	1978.7	3467.7
CM layers	-	-	963.9	4.5	1096.1	5.0	1347.0	10.1	1575.8	11.0	2691.2	21.7	843.1	1354.1

* The area was calculated with a Gaussian fit using the Project Four software by WITec.

Sample name/ Analyte	Part of the stromatolitic phosphorite	$\delta^{13}\text{C}_{\text{carb}}$ (‰)	1 σ ext. err.	$\delta^{18}\text{O}_{\text{carb}}$ (‰)	1 σ ex t. err.	$\delta^{13}\text{C}_{\text{org}}$ (‰)	TOC (%)	$\Delta\delta^{13}\text{C}$ (‰)	$\delta^{15}\text{N}_{\text{TN}}$ (‰)	TN (%)	C/N atomic	P ₂ O ₅ (wt%) *	SiO ₂ (wt%)	Al ₂ O ₃ (wt%)	Fe ₂ O ₃ (wt%)	Ti (ppm)	MgO (wt%)	CaO (wt%)	K (ppm)	Sr (ppm)	Mn (ppm)	Mg/ Ca	Mn /Sr
UV0602	bulk											28.3	16.29		0.28		2.38	41.09	794	232	244	0.0	1.1
UV0602a	column	-0.6	0.1	-13.2	0.2	-21.6	0.29	-21.0															
UV0602b	intercolumn	-0.1	0.1	-13.5	0.1	-20.0	0.11	-19.9															
UV0602c	column	-0.9	0.4	-11.7	0.4	-13.8	0.72	-12.9															
UV0602d	column					-15.1	0.33		0.8	0.05	7.7												
UV0602e	column					-18.5	0.44																
UV0602f	intercolumn					-18.4	0.13		1.5	0.06	2.5												
UV0603	bulk											0.04	1.01	0.19	0.73	28	13.39	22.13		84	933	0.5	11.1
UV0603a	column	-2.4	0.6	-13.9	1.7	-12.3	1.29	-9.9															
UV0603b	intercolumn	-0.5	0.2	-11.7	0.1	-16.7	0.22	-16.2															
UV0603c	column	-2.7	0.8	-13.7	0.9	-14.7	0.90	-12.0															
UV0603d	column					-15.8	0.98																
UV0603e	column					-14.7	1.29																
UV0603f	intercolumn					-18.4	0.10		-1.2	0.06	1.9												
UV0603g	column					-14.7	0.40																
UV0604	bulk											6.09	34.59	0.22	0.55	27	10.65	25.07		95	1364	0.4	14.3
UV0604a	column	-1.1	0.7	-14.2	0.5	-39.4	0.29	-38.3															
UV0604b	intercolumn					-28.1	0.24																
UV0604c	column					-24.4	0.12																
UV0604d	column					-32.1	0.17																
UV0604e	intercolumn					-19.9	0.13		0.3	0.05	3.0												
UV0605	cream dolomite	-0.1	0.2	-14.6	0.9																		
UV0801a	intercolumn	0.3	0.2	-14.4	0.3	-19.3	0.11	-19.7	0.5	0.05	2.6												
UV0801b	column	-0.3	0.2	-13.8	0.3	-24.9	3.00	-24.6															
UV0801c	column					-13.8	0.41																
UV0801d	column					-17.4	0.17																
UV0801e	intercolumn					-20.9	0.09		0.8	0.07	1.5												
UV0801f	intercolumn					-19.6	0.06		2.7	0.04	1.8												
UV0805a	intercolumn					-32.2	1.56																
UV0805b	column	0.0	0.4	-12.1	0.4	-17.0	0.15	-17.0															
UV0806	strom. Dolomicrite	1.3	0.2	-13.3	0.3	-22.0	0.06	-23.3															
UV0807a	intercolumn	0.7	0.2	-15.0	0.3	-13.0	0.09	-13.7	0.2	0.03	3.5												
UV0807b	column	0.4	0.3	-14.9	0.3	-15.5	2.25	-15.9															
UV0808	bulk											9.40	9.94	0.42	0.28		13.65	33.91	1463	146	460	0.3	3.2
UV0808a	intercolumn	0.4	0.2	-15.8	0.3	-19.1	0.04	-19.5	1.9	0.06	0.8												
UV0808b	column	0.2	0.2	-16.4	0.3	-29.2	0.14	-29.4															
UV0901a	column					-19.1	0.26																
UV0901b	column					-15.6	0.36																
UV0901c	column					-16.1	0.12																
UV0901d	column					-15.1	0.21																
UV0901e	intercolumn					-19.2	0.18		1.8	0.06	3.5												
UV0901f	intercolumn					-15.5	0.16																
UV0901g	intercolumn					-24.3	0.10																
UV0901h	column					-28.8	0.12																
UV0902a	column					-13.0	0.29																
UV0902b	column					-17.2	0.16																
UV0902c	column					-17.7	0.15																
UV0902d	intercolumn					-16.7	0.23		0.8	0.11	2.4												

Table 3: Stable isotope composition of decarbonated micro-drilled powders from the Badagaon stromatolitic phosphorites.

* data from ICP-OES with a reproducibility better than 1%. No Na nor Rb were detected.

Table 4: Peaks detected by STXM at the C, N, and O edges

Observed peaks (eV) – Stromatolitic phosphorite	Observed peaks (eV) – Black shale	Assigned transition	Possible molecular functional groups (references)
285.3	285.0 – 285.3	1s- π^*	Protonated/alkylated aromatic and PNA
286.5*	286.7	1s- π^*	C \equiv N (nitrile) (Apen et al., 1993; Kikuma et al., 1998; Dhez et al., 2003)
287.5*	287.3	1s-3p/ σ^*	C-C (aliphatic carbon) (Ishii and Hitchcock, 1988; Cody et al., 1996; Solomon et al., 2009; De Gregorio et al., 2011)
288.4-288.6*	288.4-288.6	1s- π^*	COOH (carboxylic groups), C=C (olefinic and aromatic) (Cody et al., 1996; Boyce et al., 2002; Bernard et al., 2012)
289.4			C-OH (alcohol) (Ishii and Hitchcock, 1988)
290.2*			CO ₃ (carbonate) (Benzerara et al., 2006)
291.7*	291.5-291.8	1s- σ^*	C-C (aromatic)
399.8	399.6	1s- π^*	C \equiv N (nitrile) (Shard et al., 2004; Leinweber et al., 2007) or (pyridine) (Vairavamurthy and Wang, 2002)
401.1	400.9	1s- π^*	Amidyl and/or peptidyl (Cody et al., 2011)
	403.7	1s- π^*	R-NO (nitro group) (Turci et al., 1996; Leinweber et al., 2007; Cody et al., 2011)
404.5-405.0	404.5		R-NO ₂ (nitro compound)
	530.8	1s- π^*	R-NO (nitro group) (Turci et al., 1996; Cody et al., 2011)
531.4-531.7	531.6		Ketone (Urquhart and Abe, 2002)
538.7	539.3		

* Peaks found in situ in the nanoscopic inclusions of organic matter and carbonate of the microbial mat.

Table 5: List of peaks detected by ToF-SIMS on the nano-fabricated foil of stromatilitic phosphorite from Badagaon.

Positive secondary ions			Negative secondary ions		
Peak label	Mass	counts per second	Peak label	Mass	counts per second
Mg ⁺	23.9819	1.89E-02	H ⁻	1.0102	5.92E-02
C ₂ H ₇ ⁺	30.9787	7.81E-04	C ⁻	12.0009	5.54E-03
Ca ⁺	39.9459	4.05E-01	O ⁻	15.9910	3.99E-01
PO ⁺	46.9701	1.15E-03	OH ⁻	16.9993	6.54E-02
CaO ⁺	55.9521	5.03E-02	F ⁻	18.9939	2.50E-01
CaF ⁺	58.9535	7.18E-02	C ₂ ⁻	23.9995	9.84E-03
MgO ₂ ⁺	Same as CaO		CN ⁻	26.0035	5.19E-02
PO ₂ ⁺	78.9677	4.27E-05	P ⁻	30.9697	3.85E-03
CaMgO ⁺	79.9343	4.41E-03	PH ⁻	31.9851	3.27E-03
PO ₄ ⁺	95.0351	3.49E-05	Cl ⁻	34.9794	2.05E-02
Ca ₂ O ⁺	95.9149	2.84E-02	PO ⁻	46.9605	7.77E-04
CaPO ₂ ⁺	102.9188	7.77E-03	O ₃ ⁻	47.9933	1.23E-03
Ca ₂ O ₂ ⁺	111.9069	1.99E-02	Fe ⁻	55.9412	6.79E-04
Ca ₂ O ₂ H ⁺	112.9205	1.52E-02	CaO ⁻		
Ca ₂ OF ⁺	114.9091	3.52E-02	PO ₂ ⁻	62.9663	1.51E-03
118.91 u	118.9067	3.11E-03	CaP ⁻		
124.89 u	124.8883	2.74E-03	PO ₃ ⁻	78.9678	1.72E-03
CaPO ₂ H ₃₀ ⁺	132.9373	1.02E-04	CH ₆ PO ₃ ⁻	97.0071	7.82E-04
Ca ₃ O ₂ ⁺	151.8809	4.66E-03	CaPO ₂ ⁻	103.1946	1.73E-05
158.89 u	158.8858	6.94E-03	Ca ₂ OF ⁻	114.9340	3.06E-04
Ca ₂ PO ₃ ⁺	158.8858	6.94E-03	126.93 u	126.9276	3.47E-04
Ca ₃ O ₃ ⁺ ?	167.8688	3.04E-03	196.93 u	196.9267	2.34E-02
Ca ₃ O ₃ H ⁺	168.8589	2.53E-03	CNAu ₂ ⁻	419.9258	2.69E-03
170.87 u	170.8714	7.85E-03	Au ₃ ⁻	590.8346	2.08E-03
Ca ₂ PO ₄ ⁺	174.8659	8.68E-03	Au ₄ ⁻	787.6760	3.20E-04
Bi ⁺	208.9781	2.51E-03			
Ca ₅ P ⁺	230.8309	5.76E-03			
Ca ₃ PO ₅ ⁺	286.795003	3.30E-03			
Ca ₆ PO ⁺	286.7853	3.23E-03			
Ca ₄ PO ₆ ⁺	286.795003	3.30E-03			
292.89 u	292.8870	2.67E-03			
Ca ₇ PO ₂ ⁺ or					
Ca ₅ PO ₇ ⁺	342.7382	1.90E-03			
Ca ₈ PO ₃ ⁺	398.6719	9.77E-04			
Ca ₉ PO ₄ ⁺	454.6465	4.84E-04			
Ca ₉ PO ₄ H ₄ ⁺	458.7661	5.54E-04			
Ca ₅ P ₃ O ₁₂ ⁺	484.3989	2.00E-04			
Ca ₁₀ PO ₅ H ₄ ⁺	514.5643	3.10E-04			
Ca ₆ P ₃ O ₁₃ ⁺	540.5595	5.31E-04			
Au ₃ ⁺	591.0331	3.40E-04			
Ca ₇ P ₃ O ₁₄ ⁺	596.2468	5.99E-04			
Ca ₈ P ₃ O ₁₅ ⁺	652.3487	4.59E-04			

1
2
3
4
5
6
7
8
9
10
11
12
13
14
15
16
17
18
19
20
21
22
23
24
25
26
27
28
29
30
31
32
33
34
35
36
37
38
39
40
41
42
43
44
45
46
47
48
49
50
51
52
53
54
55
56
57
58
59
60

Ca ₉ P ₃ O ₁₆ ⁺	708.1197	2.06E-04
Ca ₁₀ P ₃ O ₁₇ ⁺	764.6379	1.41E-04

For Review Only